

Article

Strain-Induced Phase Transformation Modeling of QP980 Steel and Its Application to Complex Loading Paths

Zhiqin Lv ^{1,2}, Enkai Dai ^{1,2}, Ning Guo ^{1,2}, Panpan Yuan ^{1,2}, Guoqiang Liu ^{1,2} and Bingtao Tang ^{1,2,*}

¹ School of Mechanical Engineering, Qilu University of Technology (Shandong Academy of Sciences), Jinan 250353, China; 13639423649@163.com (Z.L.)

² Shandong Institute of Mechanical Design and Research, Jinan 250103, China

* Correspondence: tbtsh@hotmail.com; Tel.: +86-531-89631132

Abstract: Quenching and partitioning (QP) steel has attracted much focus due to the effect of phase transformation induced plasticity (TRIP). However, the TRIP behavior makes it difficult to accurately predict the strain and stress distribution as well as the phase transformation behavior of QP steel. The scanning electron microscope (SEM) images of QP980 microstructure were obtained by scanned electron microscope in this study, which was characterized by the combination of lath martensite, polygonal ferrite and retained austenite. Volume fraction evolution of retained austenite with equivalent plastic strain (EPS) of uniaxial tension was obtained by electron back scatter diffraction. The phase transformation kinetics equations of QP980 were deduced based on the phase transformation model proposed by Olson and Cohen (simplified as O-C theory), considering the effects of strain rate, deformation temperature and stress state. A constitutive model on the dependence of the phase transformation was proposed to reveal the relation between metallographic characteristics and mechanical performance of QP980 steel during deformation. Users' subroutine VUMAT in ABAQUS/Explicit was implemented to describe the volume fraction of retained austenite (VFRA) under different stress states. The established phase transformation and constitutive model were applied to three kinds of complex path loading tests. The variation of retained austenite under complex strain paths was obtained and compared with the experimental results.

Keywords: QP steel; constitutive model; transformation kinetics; complex loading



Citation: Lv, Z.; Dai, E.; Guo, N.; Yuan, P.; Liu, G.; Tang, B.

Strain-Induced Phase Transformation Modeling of QP980 Steel and Its Application to Complex Loading Paths. *Metals* **2023**, *13*, 823. <https://doi.org/10.3390/met13040823>

Academic Editor: Matteo Benedetti

Received: 30 March 2023

Revised: 19 April 2023

Accepted: 20 April 2023

Published: 21 April 2023



Copyright: © 2023 by the authors. Licensee MDPI, Basel, Switzerland. This article is an open access article distributed under the terms and conditions of the Creative Commons Attribution (CC BY) license (<https://creativecommons.org/licenses/by/4.0/>).

1. Introduction

With the rapid growth of the automotive industry, lightweight high-strength steels (HSS) are getting more and more important for automobile body manufacturing. Advanced high strength steels (AHSS) are nowadays widely adopted to reduce vehicle weight and improve crashworthiness [1]. As early as 1960, Matlock et al. [2] noticed that the carbon atoms in the martensite phase would be enriched into the retained austenite phase. It was not until 2003 that Speer et al. [3] developed the quenching and partitioning process, which led to the third generation of ultra-high strength steel (UHSS) with a strength-plasticity product of 30 GPa%, known as QP steel. Overcoming the difficulties in the application of QP steel can effectively promote the lightweight process of automobiles, realize energy saving and emission reduction, and improve the safety of automobiles [4,5]. The excellent mechanical performance of QP steels is owing to the transformation of the internal carbon-rich residual austenite (RA) into martensite (RA→M) during deformation, which induces plasticity by phase transformation and effectively enhances the plasticity of the steel [6–8]. In multiphase steels, the hard and soft phases may benefit the overall strength and plasticity, respectively, through an effective partitioning of stress/flow strain among the constituent phases during deformation [9,10]. QP steels are widely used in various structural components of the vehicle body, thanks to their excellent combination of strength and ductility. They are also commonly employed as reinforcing beams in the roof

to provide improved stiffness and strength, enhancing the rollover protection performance of the vehicle.

TRIP effect is responsible for QP steel's high ductility and high strength. The phase transition dynamics model can be mainly divided into two aspects. One is the empirical model without physical meaning. Representative scholars include Angel et al. [11], Ludwigsen et al. [12], Sugimoto et al. [13,14], Shin et al. [15] and Beese et al. [16]. The other is the phase transition dynamics model with physical meaning based on the shear band interweaving theory. Representative scholars include Olson and Cohen [17,18], Stringfellow et al. [19] and Tomita et al. [20–22]. A key improvement about the TRIP effect is the kinetic model of martensitic phase transformation, which first appeared in the phase transformation model proposed by Olson and Cohen (simplified as O-C theory) [17,18], which only considered the effect of temperature and was incapable of describing the complex phase transformation behavior. A phase transformation behavior can be accurately described by Li et al. [23] based upon temperature and stress state, but not on strain rates. The model developed by Kim et al. [24], likewise, considered only the influence of temperature and stress state, resulting in the quasi-static applications.

In order to study the mechanism of martensitic transformation of QP steels, three factors were analyzed: temperature, strain rate, and stress state [25,26]. Both Hauser and Huang [27,28] assumed that raising the temperature would prevent the martensitic transformation from being induced by strain-induced transformation. Moor et al. [29] found that the yield strength of QP steels was correlated with temperature, and the strain-induced martensitic transformation temperature was above 10 °C. Feng et al. [30] designed a tensile test at −40–60 °C and found that the mechanical behavior of QP steel sheet were directly related to the ambient temperature. Since the temperature range of the test didn't cover the temperature range during the stamping process, the research had certain limitations. According to the research of Hecker et al. [31], martensitic transformations occur more quickly under high strain rate uniaxial tension ($\sim 10^3$ /s) than under low strain rate uniaxial tension ($\sim 10^{-3}$ /s) at low strain levels. However, when the strain is larger than 0.25, the adiabatic temperature rise lowers the driving force for RA → M, which leads to a significantly lower rate of martensitic transformations at high strain rates.

Stringfellow et al. [19] updated the O-C theory model for the martensite volume fraction evolution in a generalized rate form to consider the stress state as well as plastic strain and temperature. Jacques et al. [32] designed six specimens of different stress states for TRIP steel and studied the law of phase transformation under different stress states. It is demonstrated that for intermediate stress levels between uniaxial tension and biaxial tension, the transformation rate approaches a maximum value. In the instance of multiaxial loading paths at varying temperatures, Serri et al. [33] studied the volume fraction of the martensite and confirmed the stress-strain relation. In the cup drawing test, the effects of the stress state and the martensite phase transformation kinetics were examined. Utilizing the real-time measuring device of phase transformation, Beese et al. [16,34] came to the conclusion that the martensitic transformation was relevant to the stress triaxiality and the Lode angle parameter which caused a monotonic rise in the rate of martensite transformation. At ambient temperature, Shan et al. [35] used uniaxial tension, pure shear, plane strain, and biaxial tensile experiments to develop the phase transformation kinetic model while taking into account how the multiaxial stress state influences the rate of phase transformation. It demonstrated that the greater the stress triaxiality, the more unstable the retained austenite, and the martensitic transformation initiates more quickly. Based on Choi et al. [26], the martensitic transformation in the retained austenite phase typically occurred first adjacent to the restricted sections situated along the loading direction. This resulted from the local stress triaxiality being comparatively high in these constrained areas. This complex deformation condition led to different degrees of RA → M phase transformation in QP steel, which resulted in obvious differences in its mechanical properties. When type 304 stainless steel was subjected to tension-compression loading, Ishimaru et al. [36] observed a stagnated martensitic transformation behavior. They associated this

occurrence to the Bauschinger effect and the stress induced martensitic transformation mechanism. In their study [37], Zou et al. concentrated on the QP steels' martensitic transformation behavior under complicated loads (linear and cyclic loads). The transition from uniaxial tension to uniaxial compression caused a slowdown in martensitic transformation. However, the QP980 steel maintained a steady transformation behavior throughout the procedure of cyclic shear loading while the deformation mode remained unchanged.

When establishing the flow stress model of multiphase materials, the actual material microstructure and microstructure evolution during deformation were usually considered. Araki et al. [38] and Tomota et al. [39] proposed a mixed hardening criterion for the stress-strain relation of dual-phase steel from different perspectives. They showed that variations in the material's phase volume fraction would lead to changes in the stress-strain relationship. Tomita et al. [22] analyzed the effects of temperature, strain rate, and martensitic transformation on the constitutive equation under cyclic loading. According to the mixed hardening criterion, they derived the stress-strain curve of 304 austenitic stainless steel. Tsuchida and Tomota [40] determined TRIP using a micromechanics model that integrated the Mori-Tanaka mean field theory, the Eshelby inclusion theory, and the Weng's secant method [41,42]. They proposed a predictive model for calculating the relation between stress and strain in austenitic stainless steel. The model took into account the interactions between the phases within the material. A physics-based TRIP carbon steel model was created by Perlade et al. [43] to anticipate the macroscopic mechanical behavior of multi-constituent aggregates. It covered the impact of phase morphology and composition on the hardening of flow stress. They simplified the multiphase TRIP steel into a dual-phase material in which retained austenite was an inclusion phase, and established a stress-strain calculation model for TRIP steel. To represent the transformation plasticity that accompanies with the strain and stress-induced martensitic transformation, Han et al. [44] proposed a microstructure-based mathematical model. This model could better describe the stress-strain curve of the steel sheet under different strain rates. A microstructure-based FE model was created by Choi et al. [26] to forecast the complicated deformation behavior under various loading scenarios for TRIP steels. They introduced the effect of martensitic transformation kinetics into the model and successfully postulated the stress-strain curves of TRIP800. Fu et al. [45] studied the phase transformation and stress-strain curves of TRIP high-strength steel at different temperatures. The modified Gladman mixed hardening criterion could express the stress-strain relation of TRIP steel at different temperatures. Through experimentation and microstructure-based simulations, Srivastava et al. [46] examined the deformation micromechanics and phase transformation in QP980 steel. To acquire stress-strain curves using nanoindentation with a flat-punch indenter, they isolated specimens from the particular ferrite grains and martensite particles for micropillar compression tests.

Hou et al. [47] observed the strength differential (SD) effect of QP steel experimentally: not only the initial yield stress is different in uniaxial tension and uniaxial compression, but also the flow stress curves separate from each other (asymmetrical hardening). The plastic behavior under complex loading significantly differs from that in conventional mechanical testing [48]. Hou et al. [49] found the difference in the hardening behavior of QP980 steel under complex path loading conditions through biaxial non-proportional loadings tests, and the difference is related to the dependence of martensitic transformation on the stress state. Chakra et al. [50] investigated the relations between the microstructures and mechanical behaviors of austenitic stainless steel during deformation under different loading paths and found that the phase transformation and crystallographic texture development are strain and strain path dependent. Rittel et al. [51] developed a specimen named shear-tension specimen (STS) and shear-compression (SCS) to investigate the mechanical response of materials under dominant shear. Yang et al. [52] studied the combined shear-compression mechanical behaviors of metal alloy and analyzed the failure mechanism under different states of stress. In recent years, a reversal loading is regarded as a significant non-linear loading path in sheet metal forming [53,54]. In order to reveal the deformation and strain

responses of materials under different loading conditions, the digital image correlation (DIC) technology with improved efficiency of strain measurement can be used to measure the deformation and strain field of complex specimens under different states [55].

In the paper, the influence of the stress state, deformation temperature, and strain rate on the martensitic transformation behavior of QP steels, especially for the stress state dependent martensitic transformation behavior under complex loading, was studied. Based on Mohr et al. [56] flow stress-strain model related to martensitic transformation, the modified plastic constitutive equation was deduced. Users' subroutine VUMAT in ABAQUS/Explicit was implemented to describe the content of residual austenite under different stress states. The established strain-induced phase transformation model and constitutive model were applied to three kinds of complex path-loading tests. The QP980 material and the experimental methodology is discussed in Section 2. The modeling of the phase transformation taking strain rate, temperature, and stress state into account is described in Section 3. In Section 4, stress-strain model considering phase transformation is described. Finally, the verifications of martensitic phase transformation prediction under complex loading path are shown in Section 5.

2. Experimental Details and Results

The strain-induced austenite-to-martensite transformation behavior is affected by many factors, such as temperature, strain rate, and stress state during deformation. To clarify the influence of various factors on the martensitic transformation of QP980 steel, tensile tests at different temperatures, strain rates, and stress states were carried out, and the microstructure of the interrupted tensile specimens under different strains was characterized.

2.1. Microstructural Characterization

The cold-rolled QP980 steel sheets in their as-received condition from China Shandong IRON&STEEL Group Rizhao Co., Ltd. (Rizhao, China) have multiphase microstructure with 1.2 mm thickness. Their chemical compositions are summarized in Table 1.

Table 1. Chemical compositions of steel sheets used in the study (wt %).

Steel	Thickness (mm)	C	Si	Mn	P	S	Al	Fe
QP980	1.2	0.161	1.72	2.31	0.01	0.001	0.028	Bal.

The material's microstructure was characterized using a DM2700M optical microscope (Leica, Wetzlar, Germany). The specimens used for metallographic examinations were taken from the middle part of the specimens with uniaxial tension strain of 0.03, 0.06, 0.09, and 0.11, respectively. The specimens were polished with slurries of 6, 3, and 1 mm diamonds. The polished specimen was etched in 4% Nitrate solution for 8–12 s to characterize the microstructure and phases of the material.

Figure 1a witnesses the original microstructure of QP980 steel sheet. It is observed that ferrite and martensite make up QP980 steel's structure. However, owing to the limited magnification of metallographic observation, it is impossible to use an optical microscope to analyze the content and morphology of each phase in QP980 steel sheet. The etching step was performed as part of the overall microstructural characterization process, and the grain boundaries can be clearly observed in the EBSD images in Figure 1b,c.

The specimens were repolished using 6, 3, 1 mm diamond slurries and 0.05 mm alumina for EBSD analysis. Before EBSD, the last polishing process was carried out on a vibratory polisher with colloidal silica of 0.05 mm [57]. Figure 1b,c shows the microstructural composition of QP980 steel when the equivalent plastic strain (EPS) $\epsilon_{eq} = 0$ and $\epsilon_{eq} = 0.11$, in which red is retained austenite, blue is martensite, and green is ferrite. Ferrite, martensite, and retained austenite make up the morphology of QP980 steel sheets as-received, as shown in Figure 1b. In the bulk materials, ferrite is distributed uniformly, accompanied with lath-like martensite. At the grain boundaries of ferrite/ferrite and ferrite/martensite,

the preserved austenite particles can be detected. Table 2 provides a list of the volume fractions for each phase in QP980 steel sheet. The distribution of preserved austenite is evident from the EBSD investigation. The EBSD image for as-received QP980 shows that the area fraction of retained austenite found is 9.5% (as shown in Figure 1b) The volume fraction drops to 4.2% during 11% uniaxial tensile deformation (as illustrated in Figure 1c.

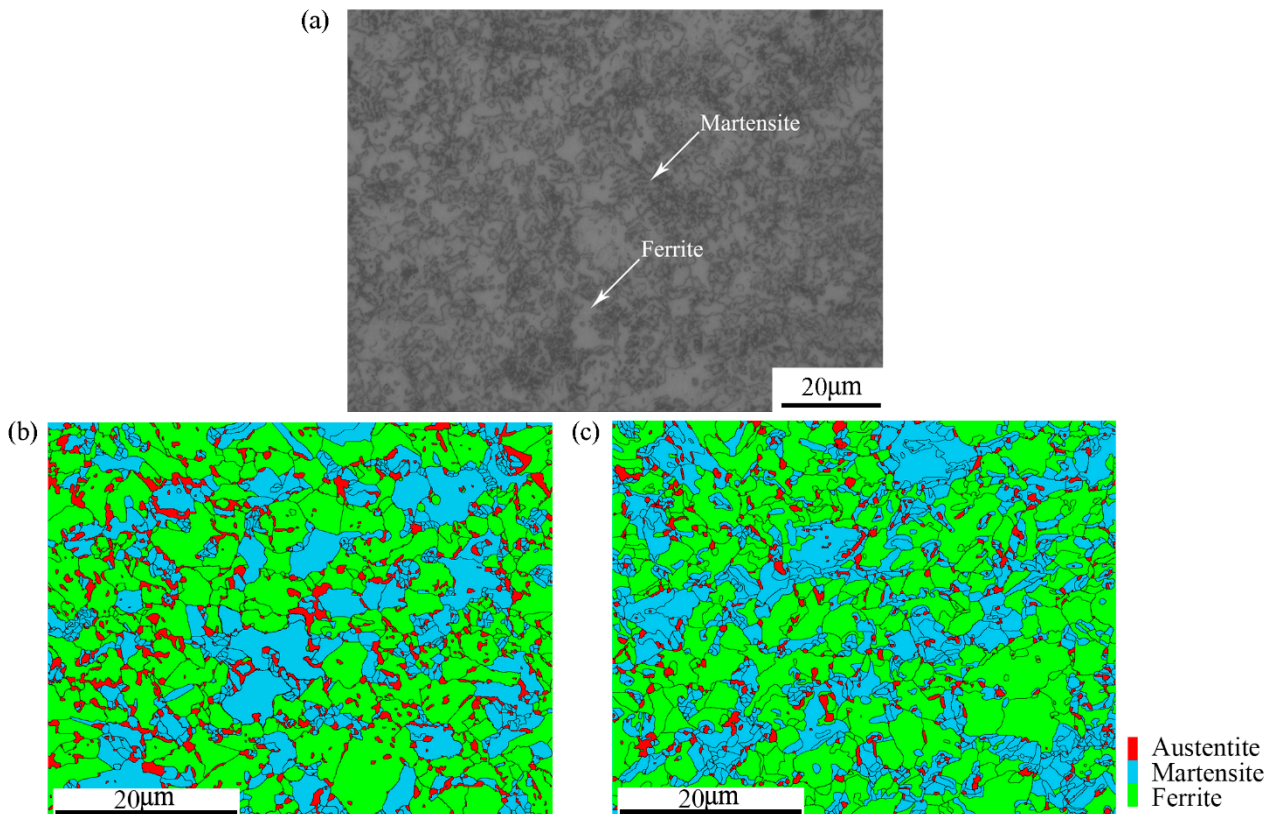


Figure 1. Microstructure of QP980 steel sheet: (a) martensite and ferrite are characterized by OM (1000×); (b) EBSD characterization of QP980 steel when $\varepsilon_{eq} = 0$; (c) EBSD characterization of QP980 steel when $\varepsilon_{eq} = 0.11$.

Table 2. Fractions of phase volume (%) of the QP980 steels ($\varepsilon_{eq} = 0$ and $\varepsilon_{eq} = 0.11$).

Phase Volume Fraction	V_{γ}	V_M	V_F
$\varepsilon_{eq} = 0$	9.5	57.8	32.7
$\varepsilon_{eq} = 0.11$	4.2	63.1	32.7

To quantitatively analyze the phase transformation process, X-ray diffraction (XRD) utilizing Cr K α radiation with a pure copper filter selected to measure the volume fraction evolution of retained austenite in QP980. The experiment used a D8-ADVANCE X-ray diffractometer (Bruker, Billerica, MA, USA) with a step size of 0.02° and a scanning angle of 40°–95° to obtain diffraction intensity data. Using the MDI Jade6.5 software, the measured initial data were filtered to deduct the background, smoothed, and phase retrieved [58]. It shows that the content of the austenite phase can be depicted by Equation (1) as follows [59]:

$$V_{\gamma} = \frac{\frac{1}{n} \sum_{j=1}^n \frac{I_{\gamma}^j}{R_{\gamma}^j}}{\frac{1}{n} \sum_{j=1}^n \frac{I_{\gamma}^j}{R_{\gamma}^j} + \frac{1}{n} \sum_{j=1}^n \frac{I_{\alpha}^j}{R_{\alpha}^j}} \quad (1)$$

with R_{γ}^j was the theoretical intensity value of the “ γ ” phase (hkl) surface, I_{γ}^j was the cumulative intensity value, n represents the number of “ γ ” phase (hkl) surfaces [60].

The martensite volume fraction under different strain conditions was obtained using Equation (1). The VFRA detected in the XRD for as-received QP980 is 10.38%. VFRA drops to 5.22% at the end of 13% uniaxial tensile deformation as shown in Figure 2. The VFRA, which is lower than the XRD result, suggests that the VFRA measured by EBSD was underestimated. This can be caused by the degradation of residual austenite during sample preparation or by a significant portion of austenite films being too thin to be resolved by EBSD [61,62]. For the investigation and modeling of martensitic transformation behavior, we employed the XRD results in the study.

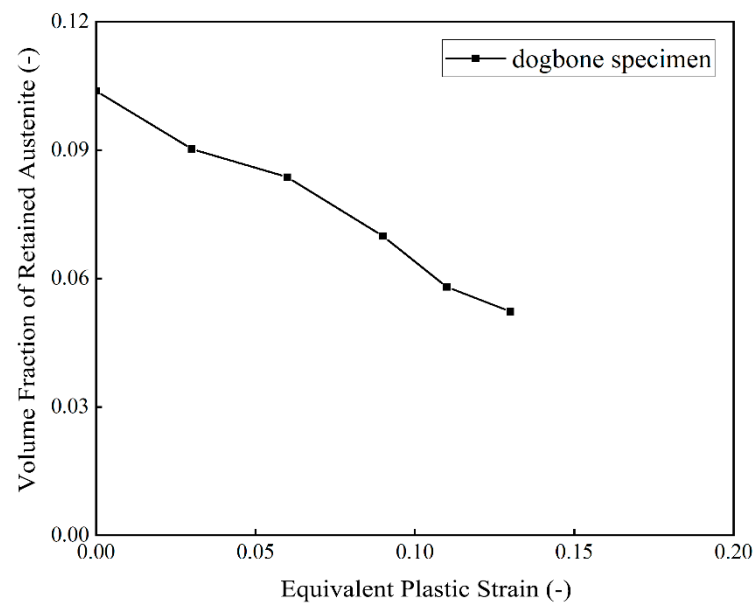


Figure 2. QP980 steel variation in retained austenite with EPS under uniaxial tension.

2.2. Mechanical Tests

2.2.1. Tensile Tests at Different Temperature and Strain Rates

According to ASTM-E8 M, specimens for uniaxial tensile testing were cut from the sheet along the direction of rolling to ascertain the macroscopic flow characteristics. Under varied strain rates and six ambient temperatures (25, 50, 70, 110, 140, and 180 °C), specimens were stretched under uniaxial tension. Digital image correlation (DIC) technique was employed during tensile testing for strain measurements to evaluate the deformation behavior of the samples under different temperature conditions. X-ray diffraction (XRD) analysis was conducted on the interrupted tensile specimens after tensile testing to further analyze the phase evolution in response to temperature impacts. In the case of low strain rates (0.0002, 0.002, 0.02 and 0.1/s), the mini tensile specimen shown in Figure 3e was selected, while in the case of high strain rates (1, 5, and 10/s), the medium tensile specimen shown in Figure 3f was used. The specimen was kept in the resistance heating furnace for 20 min before the tension was applied to guarantee thermal equilibrium at the desired temperature. Then, in the furnace with a PID temperature control unit, tensile tests were implemented. To produce specimens with various degrees of plastic strain, interrupted tensile tests were also conducted. Next, it was possible to acquire the retained austenite evolution with plastic strain. Table 3 shows the velocity of the crosshead of the specimens under different strain rates.

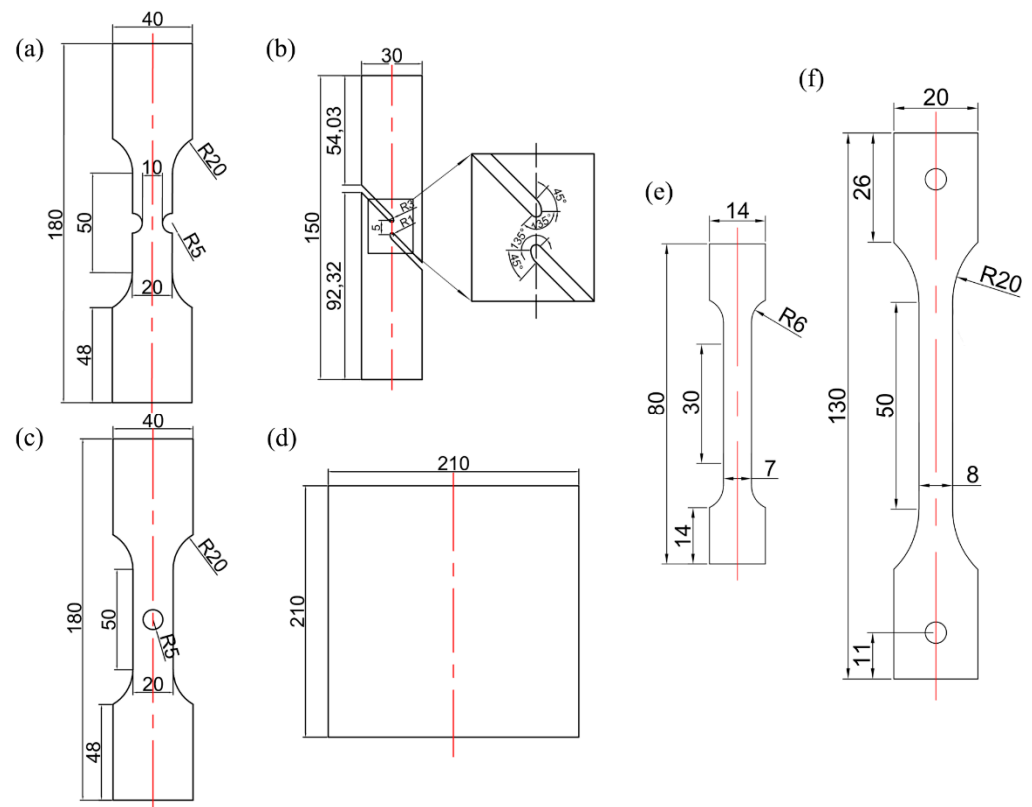


Figure 3. Shape and size of specimens: (a) notched; (b) shear; (c) central hole; (d) Nakajima specimen; (e) mini tensile specimen; (f) medium tensile specimen.

Table 3. The crosshead's velocity for various tensile specimens (mm/min).

Specimen Type	Strain Rates (/s)							
	0.0002	0.002	0.02	0.1	1	5	10	
Central hole	0.1							
Notched	0.2							
Shear	0.2							
Nakajima	18							
Mini tensile specimen	0.36	3.6	36	180				
Medium tensile specimen					300	1500	3000	

This study employed DIC technology to record strain evolution. On the specimens' one side surface, a random pattern was meticulously sprayed. A GOM ARAMIS 2017 (GOM GmbH, Braunschweig, Germany) adjustable 6 M tracked the motion of the dispersed points and as a result, recorded the displacements. Five images with a resolution of 2750×2200 were taken every second by the left and right ARAMIS 2017 cameras. The spatial resolution for the test was set at 15 pixels per millimeter. The load cell and the acquisition of the signals from the distorted pattern were both activated simultaneously and evaluated at the same sample frequency. The use of narrow-band blue light technology allows for the rapid digital recording of the surface geometry of physical objects by filtering away interfering ambient light during image acquisition. The strain field on the surface of the specimen was then obtained by computing the displacement field of the speckle using professional software called ARAMIS 2017.

2.2.2. Tensile Tests under Different Stress States

Four different types of tensile specimens, including uniaxial tension, pure shear, plane strain tension, and biaxial tension, were created as illustrated in Figure 3a–d to explore the deformation-induced martensitic transformation of QP980 steel sheet under various stress states. The biaxial tension deformation mode was realized by Nakajima hemispherical punch bulging experiment, and the experimental platform was EC600 (Genbon, Jiading District, Shanghai, China) hydraulic sheet forming machine. The other three deformation modes were realized by an electronic universal testing machine. In order to fully understand how retained austenite transformed into martensite under various deformation processes, X-ray diffraction was selected. The experimental temperature and strain rate were set to 25 °C and 0.0002/s, respectively. The crosshead's velocity for various tensile specimens is shown in Table 3. The designation of 'mm/min' units for the crosshead's velocity in Table 3 refers to the velocity at which the tensile specimens are deformed during the tensile testing process, which is consistent with the tensile speed of the specimens being tested.

3. Modeling of the Phase Transformation

The martensitic phase transformation kinetic model is used to describe the factors related to the transformation of retained austenite to martensite, which is very important for the study of phase transformation behavior and subsequent mechanical behavior of high-strength steel. This section follows the principle from simplicity to complexity and describes the step-by-step introduction of three phase transformation-related variables: temperature, strain rate, and stress state. Finally, a phase transformation kinetic model suitable for considering the actual forming process is proposed, which is used to describe and predict the strain-induced martensitic transformation behavior of QP980 steel.

3.1. Temperature-Dependent Phase Transformation Kinetic Model

The stress state and carbon content are presumptively constant throughout the investigation. A simplified kinetics model based upon the pioneering work of Sherif et al. [63] is presented to consider the impact of ambient temperature and the temperature rise caused during deformation. The amount of transformable retained austenite, the magnitude of the plastic strain, and the austenite stability parameter K all contribute to the definition of the martensitic transformation rate, i.e., the differential of the VFRA versus the macroscopic plastic strain. First, it was reasonable to suppose that the temperature of the specimen would remain constant at a static strain rate of 0.0002/s. The retained austenite stability parameter K is simplified to be a function of ambient temperature in order to consider the effect of increased temperature on martensitic transformation:

$$K(T) = \frac{1}{g(T)} = \frac{1}{k_1 T_0 + k_2} \quad (2)$$

$$\frac{df_\gamma}{d\bar{\epsilon}_{eq}} = \frac{1}{k_1 T_0 + k_2} f_{\gamma_0} \bar{\epsilon}_{eq}^\alpha \quad (3)$$

where $g(T)$ is the temperature dependent function. k_1, k_2 are constants. $\bar{\epsilon}_{eq}$ is the EPS. α is a parameter that relies on the material property and is regarded to be dependent on the strain partitioning in the multiphase steel. K is a parameter for retained austenite stability. The value of K depends on the variables that affect the TRIP effect, such as the stress state, strain rate, temperature, carbon composition, etc. The initial VFRA, denoted as f_{γ_0} , is considered to be a constant value of 10.38%. T_0 is the ambient temperature. The kinetics model under isothermal conditions can be derived by integrating Equation (3) with the boundary condition of a preliminary VFRA of 10.38%. The resulting equation is as follows:

$$f_\gamma = f_{\gamma_0} \exp \left[-\frac{\bar{\epsilon}_{eq}^{\alpha+1}}{(k_1 T_0 + k_2)(\alpha + 1)} \right] \quad (4)$$

To determine the fitting value of α using the least-square approach, a tension test at a strain rate of 0.0002/s and 25 °C is used as a reference [64]. Then, using six sets of experimental data, i.e., 25, 50, 70, 110, 140, and 180 °C, k_1 and k_2 are computed. The fluctuation of the retained austenite volume fraction with EPS at different temperatures is shown in Figure 4. With growing plastic strain, it can be seen that the VFRA declines. As the ambient temperature increases, the growth rate of martensitic transformation slows down. There is a strong agreement between the experimental data and the presented analytical model in Equation (4) across a wide range of temperatures.

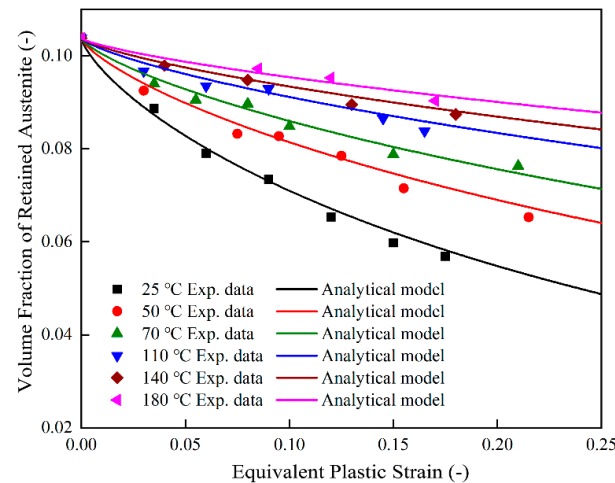


Figure 4. Comparisons of model prediction results of retained austenite evolution at various deformation temperatures.

3.2. Kinetic Model for the Phase Change That Depends on Temperature and Strain Rate

Since the analytical model obtained in Section 3.1 is only suitable for isothermal conditions, a strain-induced phase transformation model depending on temperature and strain rate will be established. As the strain rate rises up, the heat exchange between the plastic work generated during the deformation of the material and the surrounding environment will become shorter, and the heat of the material itself will be too late to dissipate and cause temperature changes, so it is no longer an isothermal process. The macroscopic temperature rise expression of the specimen is shown in Equation (5), with h denotes the coefficient of equivalent heat transfer, A and v represents the surface area and the gauge section volume of the standard tensile specimen, respectively. $\Delta\varepsilon$ and $\dot{\varepsilon}$ is the increment and strain rate. C represents the material specific heat capacity, ρ is the material density, σ is the true stress, and β is the Quinney-Taylor coefficient. The detailed parameters are shown in Table 4. The macroscopic temperature rise considering strain and strain rate effect is expressed by the following formula [65]:

$$\Delta T = \frac{\beta \int_0^{\varepsilon} \sigma d\varepsilon}{C\rho + \frac{hA\Delta\varepsilon}{v\dot{\varepsilon}}} \quad (5)$$

where ΔT stands for the macroscopic temperature rise detected by an infrared thermography system, which may also be easily addressed by a polynomial formula that includes strain and strain rate. Thus, the macroscopic temperature rise is obtained by fitting the experimental data with the expression shown in Equation (5). The martensitic transformation kinetics taking into account temperature evolution throughout plastic deformation at quasi-static strain rate is presented in Equation (6), which is derived upon the formula of transformation kinetics model at isothermal condition.

$$f_Y = f_{Y_0} \exp \left\{ - \int_0^{\varepsilon_{eq}} \frac{\varepsilon_{eq}^{\alpha}}{k_1(T_0 + \Delta T) + k_2} d\varepsilon_{eq} \right\} \quad (6)$$

Table 4. Parameters used in the temperature rise formula.

C	Specific Heat	485 J/kgK
ρ	Density	7850 kg/cm ³
β	Coefficient of Quinney-Taylor	0.9
v	Volume of the gauge section	2.52×10^{-7} m ³
A	Area of the gauge section	2.1×10^{-4} m ³

The scattered data shown in Figure 5a,b illustrate the evolution of VFRA with EPS. It demonstrates that the distribution of retained austenite is significantly influenced by the strain rate. The predictions of retained austenite vs. plastic strain at different strain rates are illustrated in Figure 5a, and the solid lines demonstrate that merely taking into account macroscopic temperature rise is insufficient to capture the apparent variation in transformation behavior induced by strain rate effect. In order to enhance this model, we thus considered the influence of microscopic temperature rise. As previously mentioned, a high strain rate caused the temperature gradient (i.e., microscopic temperature increase) in the material. The actual temperature that the martensitic transformation occurs may be underestimated. Therefore, to take account of this martensitic transformation temperature induced by strain rates, retained austenite stability parameter K considers strain rate by introducing the strain rate dependent expression of $h(\dot{\varepsilon})$ in Equation (7):

$$h(\dot{\varepsilon}) = 1 + k_3 \ln(\dot{\varepsilon}/\dot{\varepsilon}_0) \quad (7)$$

with k_3 is a constant, the reference strain rate is defined as $\dot{\varepsilon}_0$, whereas $\dot{\varepsilon}/\dot{\varepsilon}_0$ is the dimensionless strain rate.

It is assumed that the reference strain rate of 0.0002/s is a static strain rate. The model's parameters, which are presented in Table 5, were optimized using the least-squares approach. The QP980 transformation kinetic model was then enhanced and shown in Equation (8) for quasi-static strain rate and non-isothermal conditions.

$$f_\gamma = f_{\gamma_0} \exp \left\{ -\frac{1}{1 + k_3 \ln(\dot{\varepsilon}/\dot{\varepsilon}_0)} \int_0^{\varepsilon_{eq}} \frac{\varepsilon_{eq}^\alpha}{k_1(T_0 + \Delta T) + k_2} d\varepsilon_{eq} \right\} \quad (8)$$

Table 5. Normalized stress triaxiality and Lode angle parameter.

Stress State	η	$\bar{\theta}$
Uniaxial tension	0.3343	0.9602
Shear	0.0344	0.0394
Plane stain	0.5391	-0.1731
Biaxial tension	0.6653	-0.9492

The evolution of retained austenite vs. EPS as anticipated by Equation (8) is depicted in Figure 5b by the solid lines. The reliability of the improvements is demonstrated by comparisons of experimental data and predicted outputs. Our prior research shows that during the deformation with quasi-static strain rate, the enhanced thermal effect with rising strain rate prevails, leading to lower retained austenite transformation. However, the thermal influence would practically remain constant attributed to identical mechanical work while the strain rate is larger than 0.1/s. In the meanwhile, the positive influence of strain rate on martensitic transformation predominates. Accordingly, we take the temperature gradient function $h_1(\dot{\varepsilon})$ to be constant at 0.1/s strain rate under adiabatic conditions. By introducing another function, $h_1(\dot{\varepsilon})$, we are able to alter the standard temperature gradient function as below:

$$h_1(\dot{\epsilon}) = 1 + k_3 H_1(\dot{\epsilon}) \ln(\dot{\epsilon}/\dot{\epsilon}_0) \tag{9}$$

$$H_1(\dot{\epsilon}) = \begin{cases} 0 & \dot{\epsilon} \leq 0.0002/s \\ 1 & 0.0002/s < \dot{\epsilon} < 0.1/s \\ \frac{\ln(0.1/0.0002)}{\ln(\dot{\epsilon}/0.0002)} & 0.1/s \leq \dot{\epsilon} \end{cases} \tag{10}$$

where $H_1(\dot{\epsilon})$ is expressed in parametric form. The range of strain rate $\dot{\epsilon} \leq 0.0002/s$ and $\dot{\epsilon} > 0.1/s$ is used to define the limits of isothermal and adiabatic conditions, respectively. An equation was presented to consider the positive strain rate influence during plastic deformation with high strain rates. The austenite stability function K is improved by introducing a solely strain rate dependent function $s(\dot{\epsilon})$. Equation (11) shows the revised austenite stability function: The evolution of retained austenite vs. EPS is depicted in Figure 5d by the solid lines. Figure 5a,b focuses on the effect of macroscopic temperature rise on the martensitic transformation behavior at lower strain rates. However, at strain rates of 1/s, 5/s, and 10/s, the material undergoes rapid plastic deformation, resulting in rapid temperature rise due to inadequate heat dissipation. Therefore, Figure 5c was included to show the combined effect of macroscopic and microscopic temperature rise on the martensitic transformation behavior at higher strain rates. Figure 5d represents the combined effect of macroscopic and microscopic temperature rise, as well as the increasing strain rate, on the martensitic transformation behavior. The four graphs in Figure 5 represent a progressive sequence, and the fitting result is shown in Figure 5d.

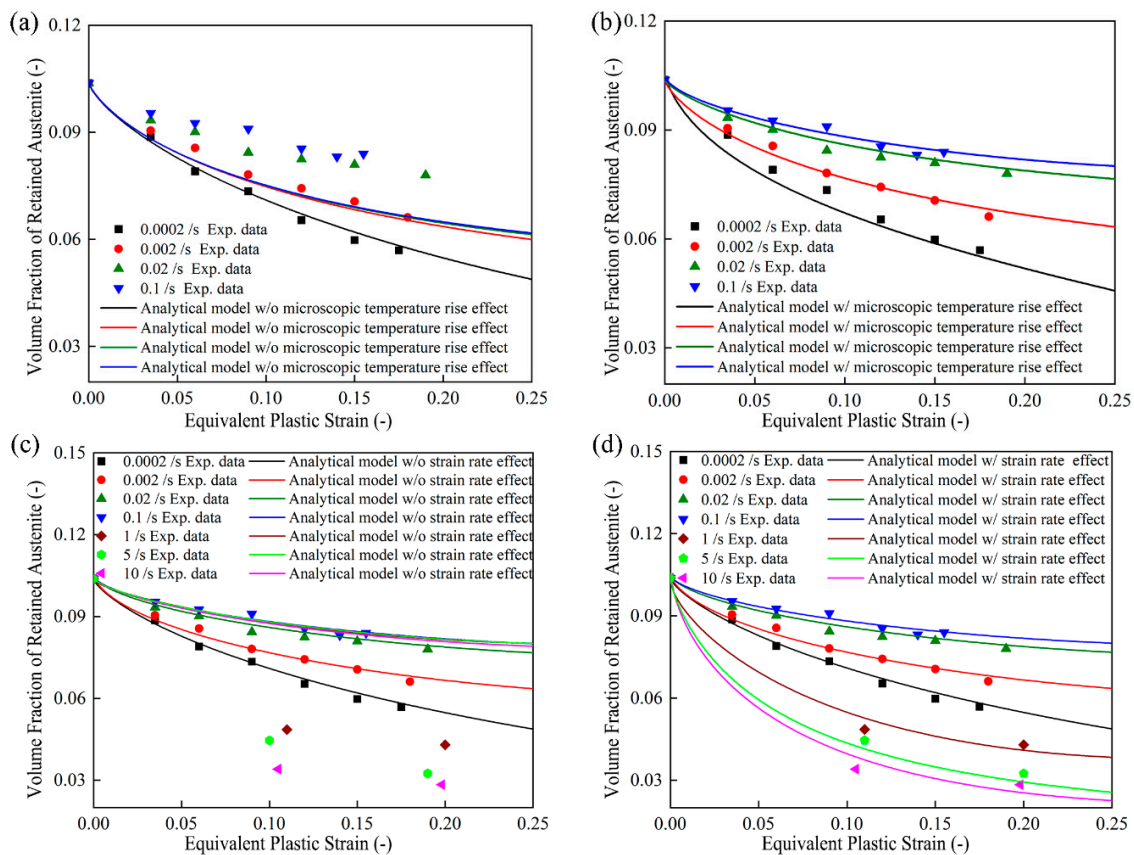


Figure 5. Analytical prediction of temperature and strain rate dependent VFRA: (a) taking into account effect of macroscopic temperature rise only; (b) taking into account effects of both macroscopic and microscopic temperature rise; (c) taking into account effect of temperature rise only; (d) taking into account effect of temperature rise and strain rate.

$$K(T, \dot{\epsilon}) = \frac{s(\dot{\epsilon})}{g(T)h_1(\dot{\epsilon})} \quad (11)$$

$$s(\dot{\epsilon}) = 1 + k_4 H_2 [\ln(\dot{\epsilon}/0.1)]^{k_5} \quad (12)$$

$$H_2(\dot{\epsilon}) = \begin{cases} 0 & \dot{\epsilon} \leq 0.1/\text{s} \\ 1 & \dot{\epsilon} > 0.1/\text{s} \end{cases} \quad (13)$$

where $s(\dot{\epsilon})$ identifies the positive strain rate influence on martensitic transformation. k_4 , k_5 are constants, which are used to fit the experimental data of martensitic transformation behavior, at strain rates of 1, 5 and 10/s. For QP980 steels, the revised martensitic transformation kinetics model fits the experimental data across a wide range of strain rates, by taking into account the influence of temperature and positive strain rates on martensitic transformation.

3.3. Stress State Dependent Phase Transformation Kinetic Model

Four typical sheet metal specimens, i.e., pure shear, uniaxial tension, plane strain, and biaxial tension, were used in the tests to examine the martensitic transformation behavior of QP980 steel under various stress conditions. For TRIP steel, Kim et al. [24] postulated that the phase evolution function relies on the square of the Lode angle. The stress state of the material deformation process was quantitatively described in the study using the stress triaxiality η and the Lode angle parameter $\bar{\theta}$. The ratio of the hydrostatic stress and the von Mises equivalent stress, as shown in Equation (14), is known as the stress triaxiality η . The second invariants J_2 and third invariants J_3 of the stress deviator s , determine the Lode angle parameter $\bar{\theta}$ in Equation (15), where $J_2 = \frac{1}{2}s : s$ and $J_3 = \det(s)$ [16]. The normalized stress triaxiality and Lode angle parameters are summarized in Table 5.

$$\eta = \frac{\sigma_m}{\bar{\sigma}} \quad (14)$$

$$\bar{\theta} = 1 - \frac{2}{\pi} \arccos \left(\frac{3\sqrt{3}}{2} \frac{J_3}{\sqrt{J_2^3}} \right) \quad (15)$$

where $\sigma_m = \frac{1}{3}(\sigma_1 + \sigma_2 + \sigma_3)$ is the hydrostatic stress and $\bar{\sigma}$ is von Mises equivalent stress.

The nonlinear function $D(\eta, \bar{\theta})$, presented in Equation (16), was employed to characterize the various transformation behaviors under various stress conditions. Numerous numerical terms are included in Equation (17), such as strain rate ($s(\dot{\epsilon})$, $h(\dot{\epsilon})$), temperature-dependent behavior $g(T)$ and the stress state $D(\eta, \bar{\theta})$ dependent phase transformation behavior. The observations of the phase volume measurement during material testing under various stress state, strain rates and temperature served as the basis for the physical evidence. The function $K[T(T_0, \bar{\epsilon}_{eq}, \dot{\epsilon}), \dot{\epsilon}, \eta, \bar{\theta}]$, i.e., the retained austenite stability function, takes into account all important variables impacting martensitic transformation. The material dependent parameter α and temperature and strain rate dependent parameters k_1 – k_5 have been calibrated and tabulated in Table 6, respectively.

$$D(\eta, \bar{\theta}) = \max \left[\left(k_6 + k_7 \eta + k_8 \eta^2 + k_9 \bar{\theta} \right), 0 \right] \quad (16)$$

$$K[T(T_0, \bar{\epsilon}_{eq}, \dot{\epsilon}), \dot{\epsilon}, \eta, \bar{\theta}] = \frac{s(\dot{\epsilon})D(\eta, \bar{\theta})}{g(T)h(\dot{\epsilon})} \quad (17)$$

Utilizing the experimental observations of four various deformation modes, i.e., pure shear, uniaxial tension, plane strain, and biaxial tension, four additional model parameters k_6 – k_9 were calibrated. The Curve Fitting toolbox in MATLAB R2019a program was used to

fit the parameters k_6 – k_9 and the values were presented in Table 6. The analytical model successfully replicated the martensitic transformation behavior of the QP980 steel sheets under various stress states using calibrated parameters, as illustrated in the solid lines in Figure 6.

Table 6. Temperature, strain rate and stress state related strain-induced phase transformation model parameters.

Model Parameters	Values
α	−0.25
f_{γ_0}	0.1038
k_1	0.0141
k_2	−3.58
k_3	0.1572
k_4	1.505
k_5	0.7602
k_6	0.3871
k_7	−0.2208
k_8	3.0882
k_9	0.3493

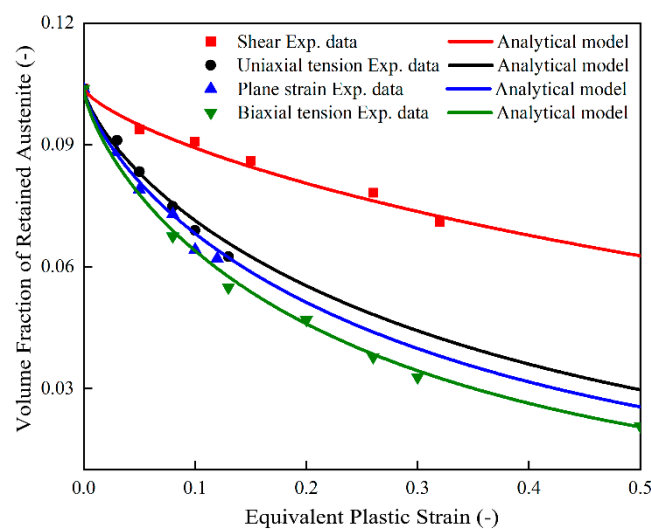


Figure 6. Comparisons of prediction results of austenite content evolution under different stress states.

To better understand the influence of various factors on the martensitic transformation behavior, the model established is now used to construct 3D surfaces and compared with experimental results for QP980 steel sheets as illustrated in Appendix A, Figures A1 and A2. It shows that the constructed 3D surface of retained austenite volume fraction can meet most of the experimental data under different strain rates and stress states.

4. Stress-Strain Model Considering Phase Transformation

The strain-induced transformation from austenite to martensite in QP980 steel is a transformation process from soft phase to hard phase, accompanied by volume expansion. Therefore, the strain hardening behavior of QP980 steel is closely related to the change of microstructure. The stress-strain model is the key to the FE simulation of forming process. QP980 steel is sensitive to temperature, strain rate and stress state because of the martensitic transformation, which will make its stress-strain behavior more complicated. In this section, based on the summary of the phase transformation dynamics model in Section 3, an in-depth study and analysis of the unique phase transformation-related strain hardening characteristics of QP980 steel will be conducted, and a macro-microcosmic coupled stress-strain model will be established.

4.1. Hardening Equation

Through the study of the stress-strain curves of QP980 steel, we know two factors of strain rate and temperature are extremely important to the phase transformation. To consider the influence of strain rate hardening and temperature softening, a macroscopic stress-strain model considering phase transformation was used. It is considered that the generation of martensite volume fraction and the strain hardening evolution determine the deformation resistance of QP980 steel. The accumulated martensitic volume and the dislocation pile-up accounts for the increment of deformation resistance $d\sigma$, and the framework is formulated in Equation (18):

$$d\sigma = H_{Swift}d\varepsilon_{eq} + H_{FM}df_{FM} \quad (18)$$

$$H_{Swift} = nk(\varepsilon_{eq} + \varepsilon_0)^{n-1}m(T)R(\dot{\varepsilon}) \quad (19)$$

$$m(T) = \exp\left[m_1\left(\frac{T - T_0}{T_m - T}\right)^{m_2}\right] \quad (20)$$

$$R(\dot{\varepsilon}) = [1 + R_1 \ln(\dot{\varepsilon}/\dot{\varepsilon}_0)] \quad (21)$$

$$df_{FM} = -df_{\gamma} = K[T(T_0, \varepsilon_{eq}, \dot{\varepsilon}), \dot{\varepsilon}, \eta, \theta] (f_{\gamma 0} - f_{\gamma}^{min}) \varepsilon_{eq}^{\alpha} d\varepsilon_{eq} \quad (22)$$

where n , k , ε_0 are the parameters of Swift strain hardening model. m_1 , m_2 are temperature parameters, R_1 is the reference parameter of strain rate. T_m denotes the melting point of the material, which is assumed to be 1750 K, and $\dot{\varepsilon}_0$ is static strain rate. T in Equation (22) denotes the instantaneous temperature, which depicts the thermal effect caused by ambient temperature and deformation-induced heating. T is considered to be the summation of ambient temperature T_0 and the temperature rise ΔT . According to Zou et al. [65], the computation of the temperature rise across a wide range of strain rate is described in Equation (5), where the constants of QP980 steel are presented in Table 4.

H_{Swift} is the Swift exponent hardening equation, which is controlled by temperature and strain rate. Its value determines the level of hardening in the material caused by dislocations, with higher values indicating higher hardening due to dislocations. $d\varepsilon_{eq}$ denotes the increment of the von Mises EPS, and df_{FM} is the volume fraction increment of the generated martensite, corresponds to a reduction in the VFRA df_{γ} in Equation (22). Deformation resistance is supposed to be a particular function of the von Mises EPS when a phase transformation is not occurring. Supposed to be constant, the second hardening modulus, H_{FM} , governs the strain hardening rate owing to the growing martensite volume fraction. H_{FM} is related to the newly formed martensite resulting from phase transformation. Its value represents the stress increment introduced by the newly formed martensite. Beese et al. [56] presented a comparable constitutive framework for isothermal and static strain rate scenarios. An empirical work hardening constitutive equation based on temperature and strain rate was proposed as three multiplicative functions in Equation (19). Traditional strain hardening of QP980 steel sheets was characterized by the Swift-type power law. As indicated in Equations (20) and (21), $m(T)$ and $R(\dot{\varepsilon})$ functions were included to respectively describe the influence of thermal softening and strain rate strengthening.

Built-in genetic algorithm in MATLAB software was used to calibrate the parameters of the developed plastic constitutive equations. Table 7 lists the optimized material parameters n , k , ε_0 , H_{FM} , m_1 , m_2 , and R_1 . Observed experimental data and estimated stress-strain curves are compared in Figure 7. Seventeen different experimental stress-strain curves agree well with the calibrated model's predictions. Figure 7d shows that the model is able to capture the significant discrepancy in equivalent stress-strain curves between various deformation conditions. It is mostly attributed to the phase transformation behavior which is stress state dependent [66]. As demonstrated in Figure 7a–c, there was a good

agreement for uniaxial tension testing in the rolling direction conducted at different strain rates and temperatures.

Table 7. Parameters in the stress-strain model.

Model Parameters	Values
n	0.142
k	1424 (MPa)
ϵ_0	0.0023
H_{FM}	2502 (MPa)
m_1	6.528
m_2	6.225
R_1	0.0065

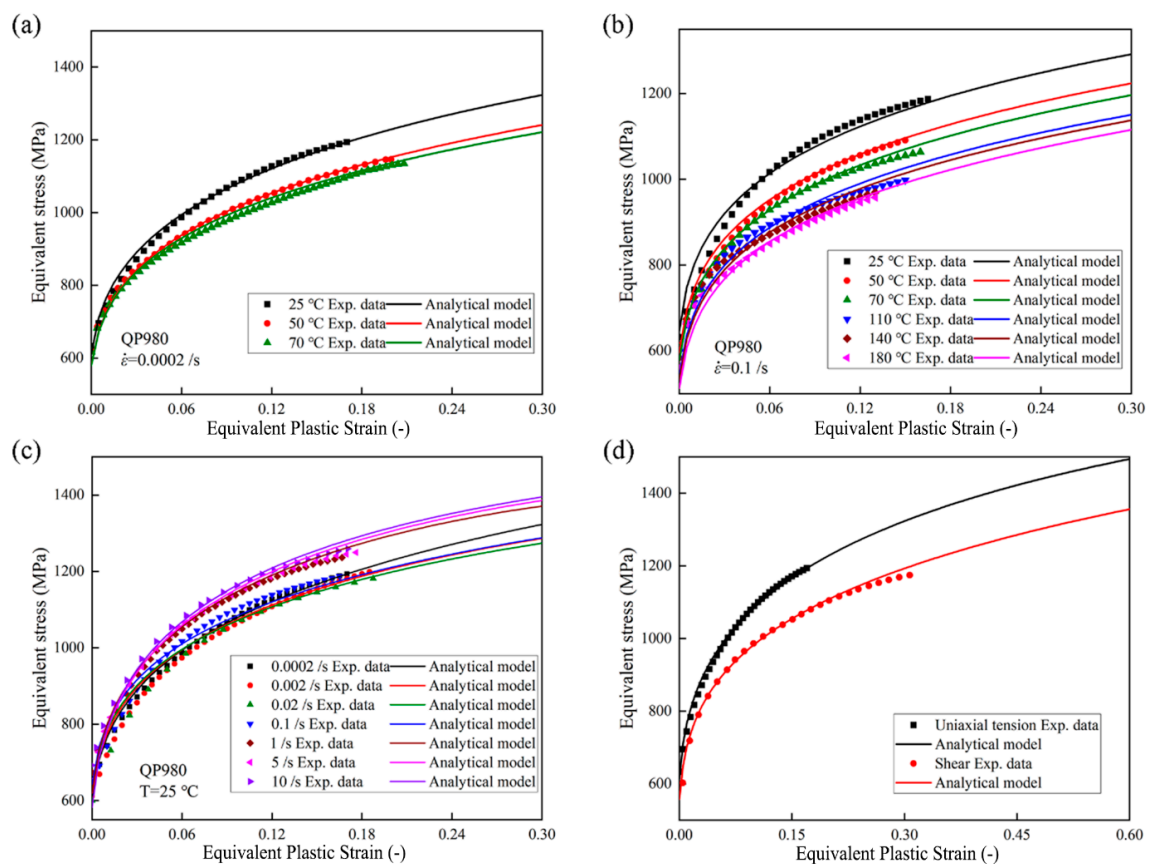


Figure 7. Analytical predictions and experimental data of equivalent stress-strain curves at various strain rates and temperature: (a) equivalent stress-strain curves at various temperature and a fixed quasi-static strain rates ($\dot{\epsilon} = 0.0002/s$); (b) equivalent stress-strain curves at various temperature and a fixed medium strain rates ($\dot{\epsilon} = 0.1/s$); (c) equivalent stress-strain curves at various strain rate and a fixed temperature ($T = 25\text{ }^{\circ}\text{C}$); (d) equivalent stress-strain curves under tension and shear stress conditions.

4.2. Finite Element Simulation

The user subroutine VUMAT was implemented in ABAQUS/Explicit to predict the martensitic transformation in different stress modes. As was illustrated in Figure 8, all specimens with different stress states were discretized with C3D8R elements. To improve computational accuracy and efficiency, one-eighth of notched and central hole specimens were utilized. A quarter model of Nakajima specimen and a one-half model of the shear specimen were created. Except for the Nakajima test, which uses 0.45 mm hexahedral meshes in the crucial zone, the FE models use 0.09 mm hexahedral meshes along the

thickness direction. As for the Nakajima tests, the punch, die, and holder are represented as analytical rigid bodies in the FE model. Additionally, since the specimen was sufficiently lubricated by a layer of soft silicon film, the friction coefficient between punch and specimen was assumed to be 0.05, while 0.5 between holder and die [67].

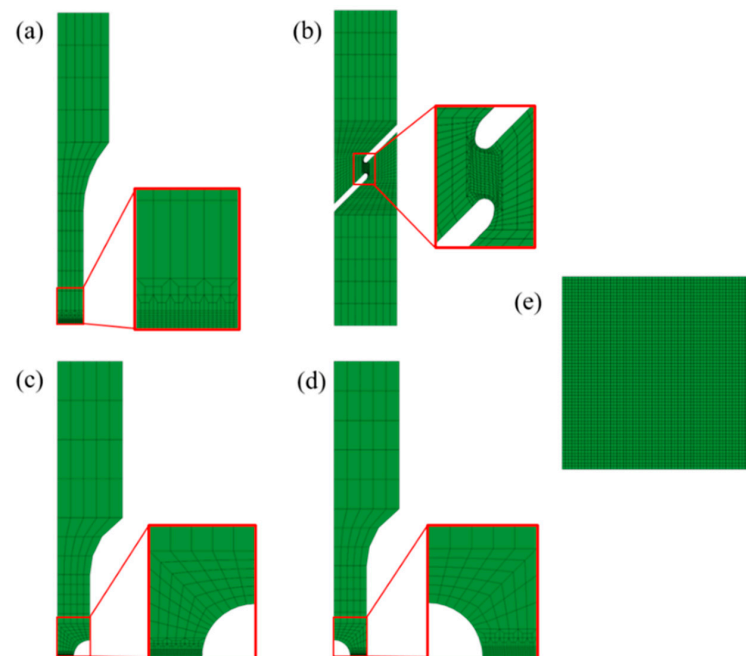


Figure 8. Meshes at ambient temperature for specimens under various stress mode: (a) Dog-bone specimen; (b) shear specimen; (c) notched specimen; (d) central hole specimen; (e) Nakajima specimen.

Using DIC technique, the strain distribution of QP980 tensile specimens was determined in different stress states. Shown in Figure 9a–d, the distribution of EPS by the FE simulation just before fracture initiation are compared with the one measured by DIC technology. It illustrates that the developed FE model can accurately depict the strain distribution during plastic deformation.

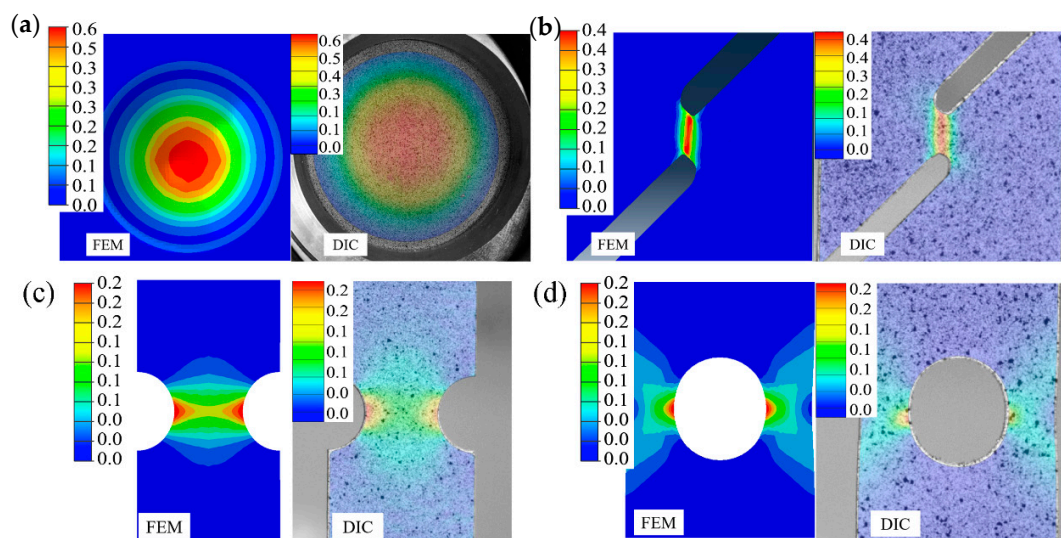


Figure 9. Comparison of strain distribution on a deformed surface in ARAMIS 2017 test (right) and FE model (left): (a) Nakajima specimen; (b) shear specimen; (c) notched specimen; (d) central hole specimen.

The evolution history of the retained austenite content is plotted in Figure 10. The FE model and the analytical model could well predict the evolution of retained austenite content with EPS in different stress states. Because of the inhomogeneous distribution of stress triaxiality in the FE model when deformation occurs, there may be a notable divergence between the FE and the analytical model presented in Figure 10a. When the equivalent strain exceeds 0.25, the stress triaxiality in the central region of the Nakajima specimen approaches 0.67, and the developed FE model can well forecast the change of retained austenite in this deformation mode.

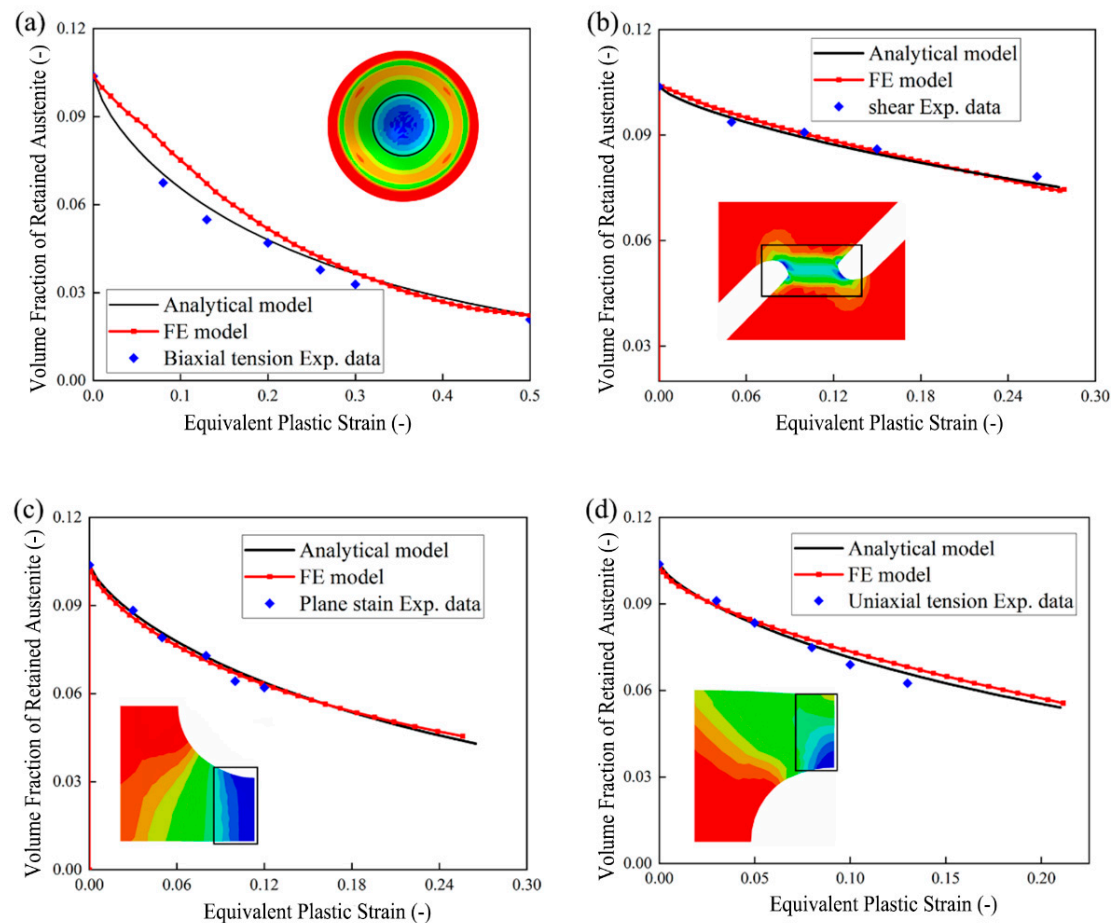


Figure 10. Comparisons of the VFRA using analytical and FE model: (a) Nakajima specimen; (b) shear specimen; (c) notched specimen; (d) central hole specimen.

5. Testing and Validation

During the stamping process of QP980 steel, the stress state of the sheet is changing all the time. In this section, three experimental scenarios for complex loading paths are presented. Based on established users' subroutine VUMAT in ABAQUS/Explicit, the martensitic transformation during the complex loading path tests can be described.

5.1. Cyclic Loading in Plane Strain

In the study, a setup was designed to supply cyclic loadings under the plane strain, as illustrated in Figure 11. Dihedral punches are used in the plane strain test setup to provide out-of-plane force to a symmetrically cut two-hole specimen. There are two chamfered circular cut-outs with diameter of 16 mm on the specimen. The gage section between two circular cut-outs is 20 mm. A dihedral punch with edge radius of 1 mm is used to apply out-of-plane loads. The plane strain test setup was equipped with a draw bead, and a blank holder force of 150 kN was employed to mount the specimen during the test. The

surface strain of the specimen was obtained using the DIC strain measurement system in the experiment. To verify the predictability of the martensitic transformation model under cyclic plane strain path, the experimental procedures are shown in Table 8.

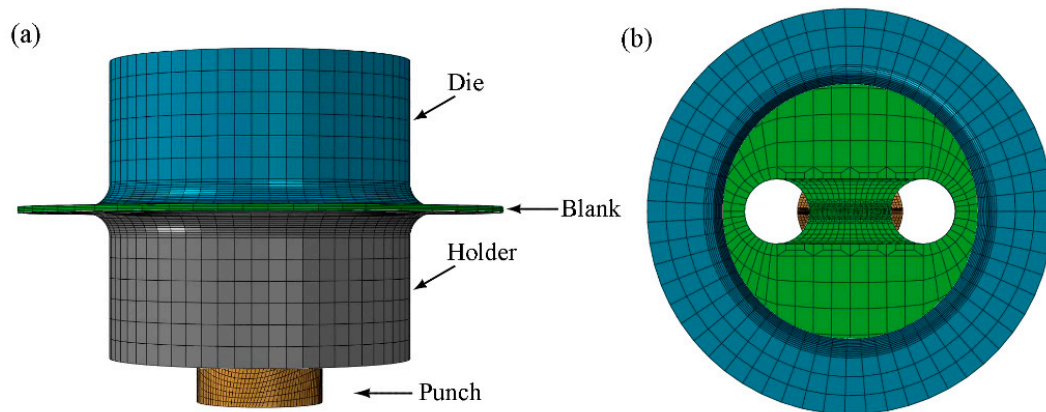


Figure 11. The FE model of the cyclic plane strain path loading: (a) front view; (b) vertical view.

Table 8. Experimental procedure for cyclic plane strain path.

Cyclic Plane Strain Path		1st Loading	1st Unloading	2nd Loading	2nd Unloading	3rd Loading	3rd Unloading	4th Loading
I	duration/s	23	17			interrupted		
II	duration/s	23	17	26.2	28		interrupted	
III	duration/s	23	17	26.2	28	37	30	interrupted
IV	duration/s	23	17	26.2	28	37	30	fracture

The cyclic loadings under the plane strain condition were modelled in the FE simulation. The FE model used linear hexahedral C3D8R solid elements with eight nodes and reduced integration. In the crucial area along the thickness direction, the FE models use hexahedral meshes with a size of 0.09 mm. During the simulations, constant velocities were applied to the specimen boundaries. The two-hole specimen was considered to be mounted on their outer boundary. Both dihedral and spherical punches were represented by rigid bodies. There was vaseline paste between the blank and the punch to be fully lubricated, so the friction coefficient between them was assumed to be 0.05. It was assumed to use a friction coefficient of 0.2 between the die and holder. The velocity of the punch was set to 12 mm/min.

The simulation results are evaluated with the experimental measurements shown in Figure 12a to show the validity of the FE model. The comparison shows that the simulated load-stroke curve fits the experimental values of the four loading-unloading cycles quite well. At the same time, the evolution of the EPS at the center of the two-hole specimen surface is extracted from the DIC data, and compared with the EPS at the same position in the simulation in Figure 12b.

Interrupted tensile tests were used to monitor the evolution of retained austenite content in case of cyclic plane strain loading [68]. XRD tests were implemented after the assigned EPS of 0.06, 0.12, 0.2 and 0.23, respectively. The distribution of the retained austenite content by the analytical model was made a comparison with the experimental results, as shown in Figure 13.

Based on the FE simulations of the two-hole specimen, the martensitic transformation characteristic of the part during forming was predicted and analyzed. The simulation results are extracted when the EPS is 0.12 during the cyclic loadings under the plane strain condition. The stress triaxiality, Lode angle parameter, EPS, and residual austenite distribution were shown Figure 14. According to the FE simulation, the evolution of retained

austenite is mainly concentrated in the central region of the two-hole specimen, which resembles the distribution of EPS. When the temperature and strain rate are determined, the transformation of retained austenite in QP980 steel is mainly related to the nonlinear function $D(\eta, \bar{\theta})$, and its value depends on the stress triaxiality and Lode angle parameter of the sheet during deformation parameter. From Figure 14a,b, it can be seen that the stress triaxiality and Lode angle parameter in the central area of the two-hole specimen are relatively stable during the cyclic loading process of the QP980 sheet, but the changes in other areas of the specimen are more complicated. Observing Figure 14d, it can be seen that only the central area of the two-hole specimen has plastic deformation, so the evolution of retained austenite is mainly concentrated in this area.

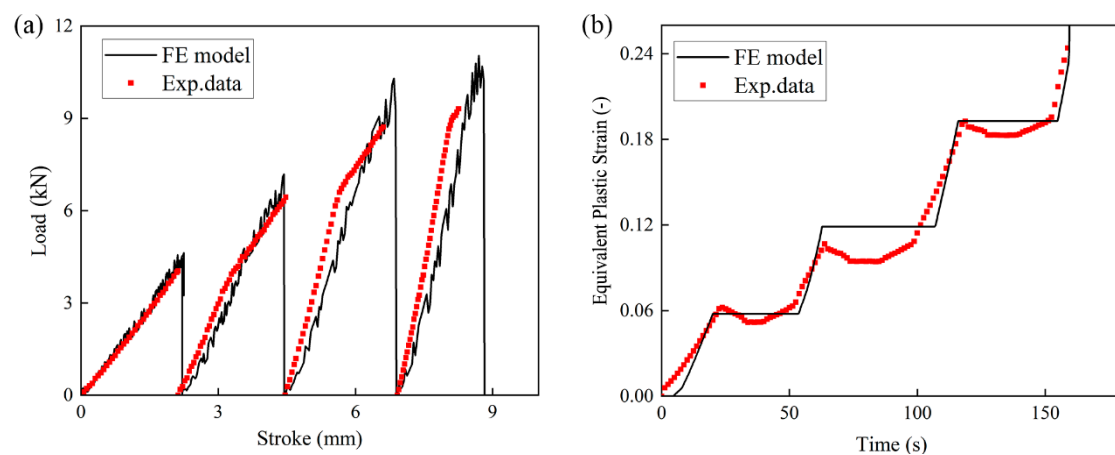


Figure 12. Comparison of cyclic plane strain loading and FE simulation: (a) Load-Stroke comparison; (b) EPS comparison at the central surface deformation area.

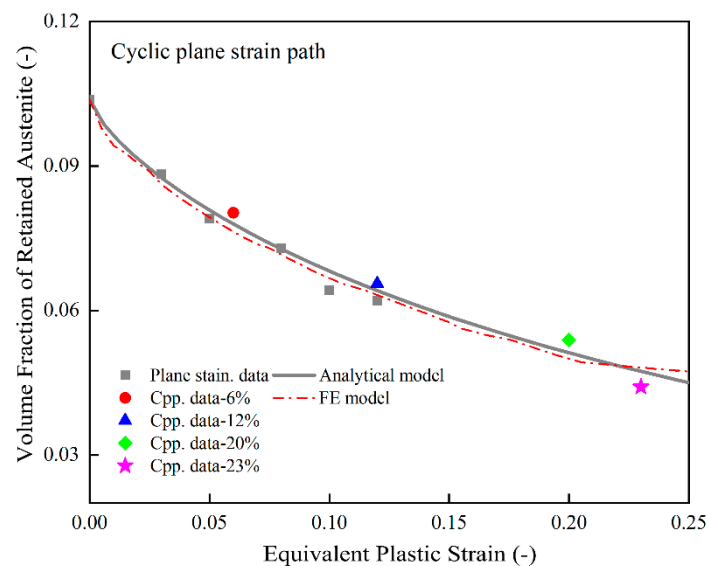


Figure 13. Variation of retained austenite with EPS of cyclically loaded plane strain specimen: these include experimental results from tests of retained austenite volume fractions at EPS of 6%, 12%, 20%, and 25%, and predictions of VFRA from analytical model and FE model.

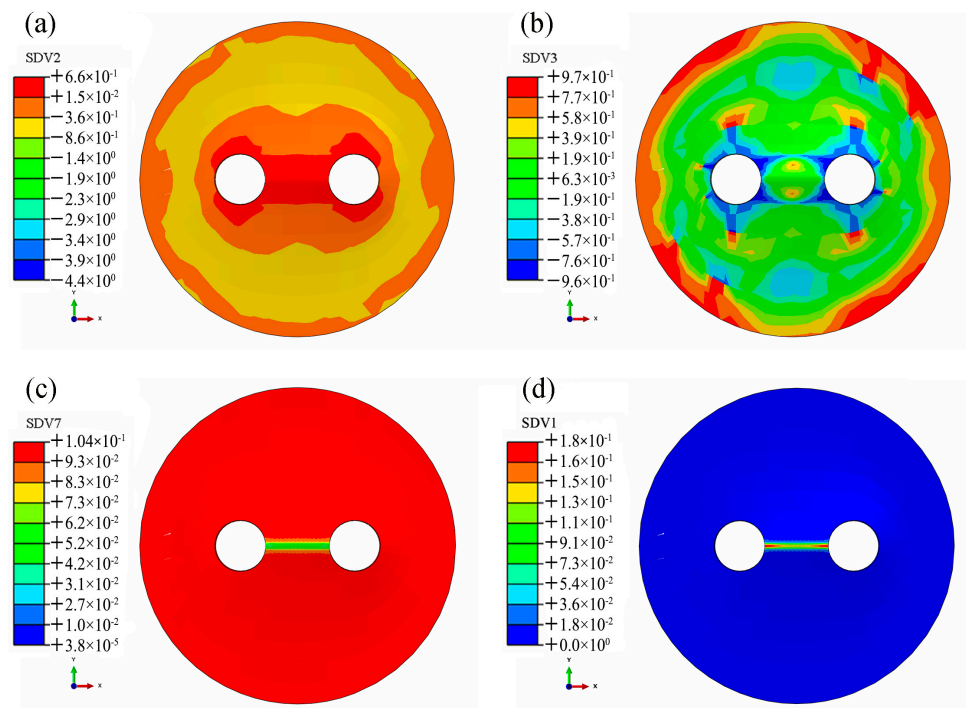


Figure 14. The FE simulated results of the two-hole specimen model after the second cyclic loading: (a) stress triaxiality; (b) Lode angle parameter; (c) retained austenite; (d) EPS.

5.2. Cyclic Loading in Shear Stress

In order to forecast the flow behavior for metal forming process, Brosius et al. [69] presented a twin bridge torsion shear test equipment. A schematic sketch with two opposing shear bridges is shown in Figure 15. One round clamping region is located in the middle, while the other is located on the outside. A plane torsional moment is transmitted through the specimen by rotating the outer clamps in opposition to the inner ones. Bridges, the only link between the interior and outside of the specimen, are subjected to strain localization as a result of the slit geometry. Two bridges are constructed symmetrically to prevent any unexpected forces or moments. Both bridges are sheared in the same manner by rotating the clamps in opposition to one another. By switching the torsional load, it appears that this specimen makes it simple to determine the cyclic behavior of materials. Therefore, in order to explore the martensitic phase transformation law of QP980 steel under the cyclic shear loading path, two sets of cyclic torsional shear experiments were designed. The loading terminated when the EPS of the bridge surface reached 0.07. The reverse loading started until the value of the EPS increased to 0.13. Similarly, another experiment was carried out until the 1st round EPS reached 0.12 and the reversed one reached 0.32.

Due to the complexity of the double-bridge shear specimen, a simplified modeling was adopted in the FE simulation, as displayed in Figure 15b. The local mesh refinement was used for the critical area of the specimen to improve computing efficiency and accuracy. The average element size in the slit geometry in the region of the bridge was selected as 0.15 mm [70]. To ensure the strain rate in the double-bridge region sufficiently low, the torsional velocity in the experiment was set to $0.04^\circ/\text{s}$. DIC strain measurement system was enforced to acquire the surface strain.

The EPS at the region of the bridge of the specimen surface was obtained in the torsion experiment and compared with simulation. As illustrated in Figure 16, the dotted lines were obtained from two torsion experiments, and the solid lines were obtained from FE simulations. The comparison shows that the simulated evolution of EPS was consistent with the experimental data during the cyclic loading in shear stress.

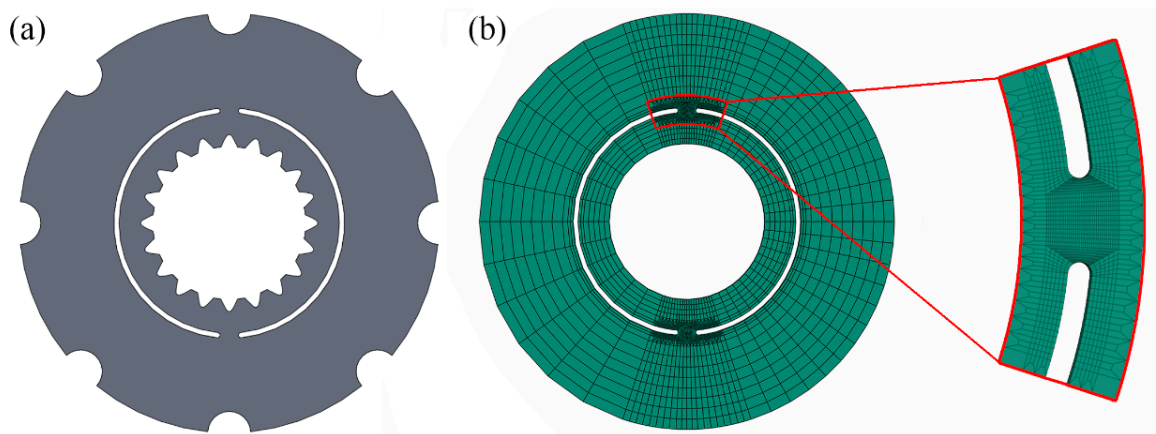


Figure 15. Schematic diagram of the twin bridge torsion shear specimen: (a) CAD model; (b) the simplified FE model.

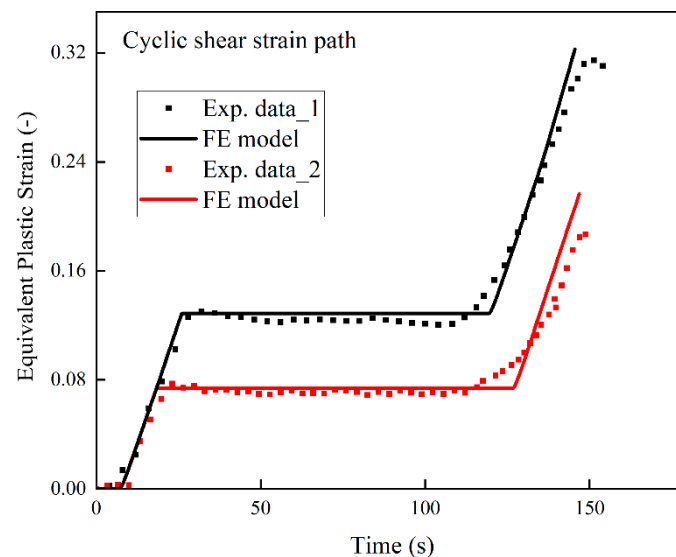


Figure 16. Comparison of the EPS evolution between simulation and experiment: these include the evolution of the EPS on the surface of the twin bridge torsion shear specimen for two experimental protocols and the evolution of the equivalent plastic strain on the surface extracted in the FE model.

The retained austenite content in the bridge area depicted by the proposed analytical model agrees well with the experimental data, as illustrated in Figure 17. When the double-bridge shear specimen is torsion, the stress triaxiality and Lode angle parameter in the shear bridge region will change. At the same time, with the increase of EPS, the content of retained austenite in this area will decrease continuously, especially in the areas with larger $D(\eta, \bar{\theta})$ values on both sides of the shear bridge. The average $D(\eta, \bar{\theta})$ value of the shear bridge surface is relatively stable, therefore, in Figure 17, the evolution history of retained austenite extracted in the FE model is not much different from the analytical model. Figure 18 shows the uniformly distributed retained austenite in the bridge area of the torsion shear specimen because of the uniformly distributed stress state and EPS during the pure shear test.

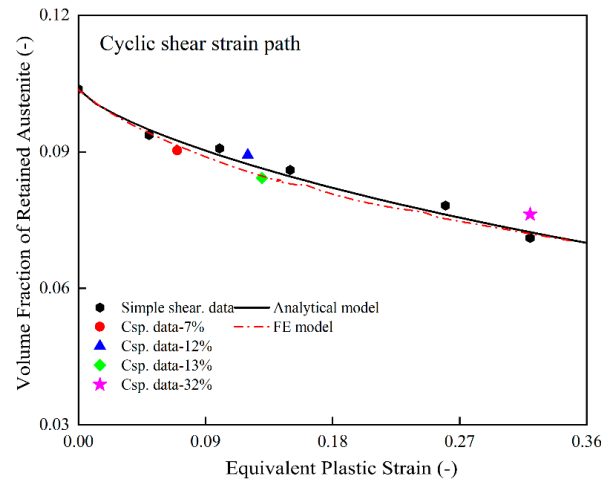


Figure 17. Evolution of retained austenite with EPS during cyclic shear strain loading: these include experimental results from tests of retained austenite volume fractions at EPS of 7%, 12%, 13%, and 32%, and predictions of VFRA from analytical model and FE model.

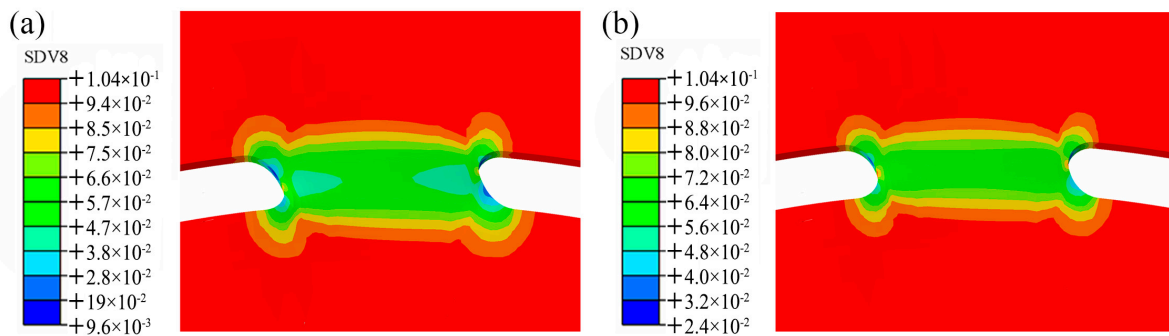


Figure 18. Distribution of retained austenite at different torsion stages in the critical area of the twin bridge torsion shear specimen: (a) $\epsilon_{eq} = 0.07$; (b) $\epsilon_{eq} = 0.12$.

5.3. Biaxial-Plane Stain/Shear Loading

To verify the predictability of the strain-induced phase transformation model under the nonlinear strain paths, the Marciniak specimens were intended to experience the biaxial pre-straining, followed by uniaxial tension or shear stress state. The prestrain of Marciniak specimen is assigned to be 0.025 and 0.05, respectively. The notched specimens and shear specimens were cut by wire electrical discharge machining (EDM) machining from the stretched Marciniak specimens and were subsequently subjected to tensile test respectively. Two interrupted tensile tests were carried out with the notched and shear specimens. The interrupted time of the tensile test is shown in Table 9. The velocity of the crosshead for the wire-cut specimens was 0.15 mm/min. The retained austenite content was measured with the XRD method, and used to verify the analytical model.

Table 9. Experimental procedure for Biaxial-plane stain/shear loading.

Nonlinear Loading Path	Biaxial Tension-Plane Stain			Nonlinear Loading Path	Biaxial Tension-Pure Shear		
I	0.025	0.06	interrupted	V	0.025	0.12	interrupted
II	0.025	0.10	interrupted	VI	0.025	0.22	interrupted
III	0.05	0.07	interrupted	VII	0.05	0.13	interrupted
IV	0.05	0.11	interrupted	VIII	0.05	0.23	interrupted

The ABAQUS/Explicit module in the FE program was used to realize the FE simulation of this experiment. A quarter geometry of a specimen was used in the FE modeling. The hexahedral grid size of the FE model has a maximum value of 1.5 mm and a minimum value of 0.3 mm. The holder, the punch, as well as the die are modeled with analytical rigid surfaces, as shown in Figure 19. In the FE simulation process, the C3D8R solid elements were used for deformed mesh of the cylindrical cup. Since there was Vaseline paste between the punch and the specimen, the friction coefficient is assumed to be 0.05. The value of friction coefficient between the die and the holder was 0.5. The velocity of the punch was set to 9 mm/min. In the experiment, DIC visualizes deformations and records strain over the entire visible specimen surface.

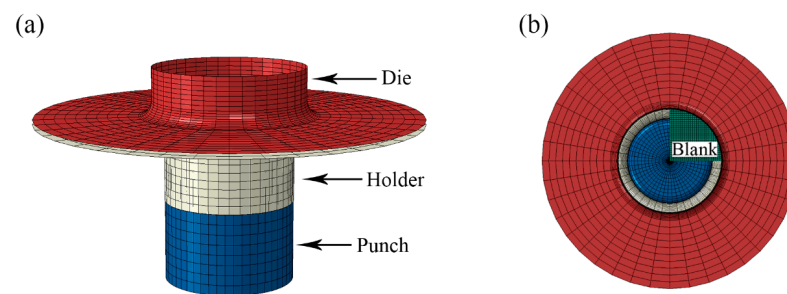


Figure 19. Marciniak test FE model: (a) front view; (b) vertical view.

The EPS, instantaneous austenite content, stress triaxiality, and Lode angle parameters during the deformation process were calculated in the FE software. Figure 20 shows the distribution of the stress triaxiality, the Lode angle parameter, retained austenite and the EPS when the stroke reaches 25 mm. Since the distribution of the EPS of the Marciniak specimen is uniform, the notched and sheared specimens obtained by wire cutting have uniform prestrain.

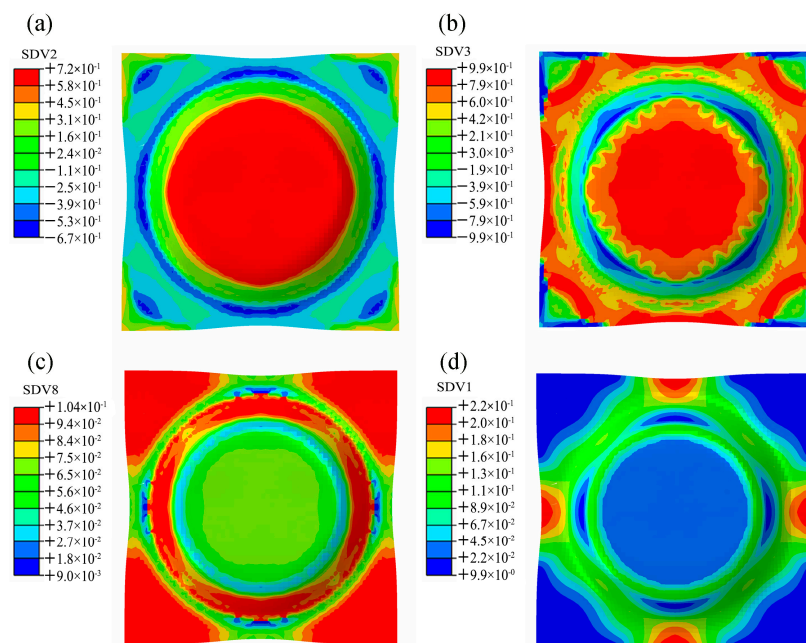


Figure 20. Marciniak simulation results when the stroke of the punch reaches 25 mm: (a) stress triaxiality; (b) Lode angle parameter; (c) retained austenite; (d) EPS.

The retained austenite content of the bulging specimen was measured by XRD method to verify the prediction accuracy of the proposed martensitic transformation model. As illustrated in Figure 21 the XY plane is intercepted at the surface of the bulge specimen in the

vertical direction. The red cross-sectional profile shown in Figure 21a is 3D curve denoted as curveL. The X-axis in Figure 21b corresponds to the length of curveL, Y-axis denotes the VFRA when the stroke of the punch reaches 25 mm, and the origin is the left endpoint of curveL in Figure 21a. The VFRA of four specific locations denoted by L1, L2, L3 and L4 is extracted and compared with XRD test data, shown in Figure 21b. It shows that the proposed martensitic transformation model can well predict the distribution of VFRA.

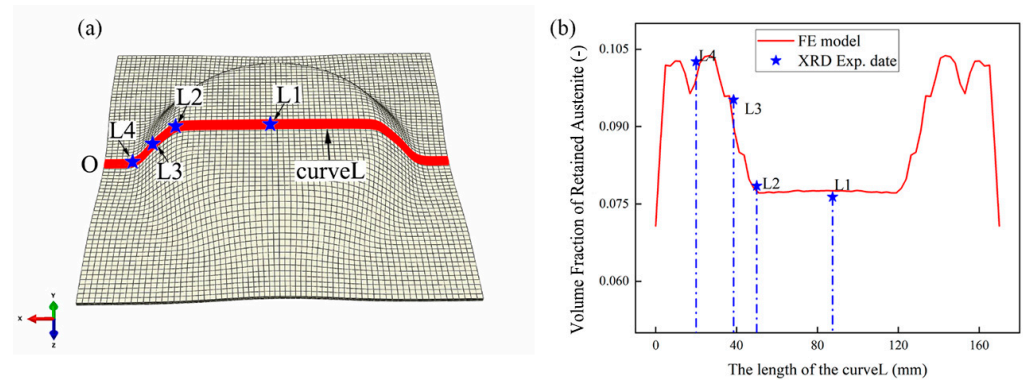


Figure 21. When the stroke of the punch reaches 25 mm, comparison between Marciniak test results and Prediction results of martensitic phase transformation by FE model: (a) schematic diagram of the location of XRD points; (b) the results of martensitic transformation predicted by FE model are compared with the experimental results.

Tensile tests were implemented with the mini notched and mini pure shear specimens which were machined by wire-electrode cutting from the pre-strained Marciniak specimen shown in Figure 22. Eight sets of interrupted tensile tests were conducted according to the experimental procedure shown in Table 9. After 2.5% pre-strain of biaxial tensile test, the specimens with the EPS of 6% and 10% under the plane strain loading (I and II) and the specimens with the EPS of 12% and 22% under the shear loading (V and VI) were obtained. Similarly, after 5% pre-strain of biaxial tensile test, the specimens with the EPS of 7% and 11% under the plane strain loading (III and IV) and the specimens with the EPS of 13% and 23% under the shear loading were obtained (VII and VIII). The retained austenite content at the positions shown in Figure 22 (blue dots) was tested by XRD and compared with the FE model. When the loading path is changed, the values of the stress triaxiality and Lode angle parameter are quite different. Likewise, a sudden change in the value of $D(\eta, \bar{\theta})$ will then lead to a change in the speed and extent of the martensitic transformation. With the continuous increase of EPS, the evolution trajectory of VFRA will be more obvious compared with the loading path unchanged. Figure 23 shows the distribution of retained austenite with EPS evolution under different loading paths. It shows that the martensitic transformation model can well predict the distribution of VFRA and accurately describe the sudden change due to the variation of the stress triaxiality and the Lode angel parameter when nonlinear strain path occurs.

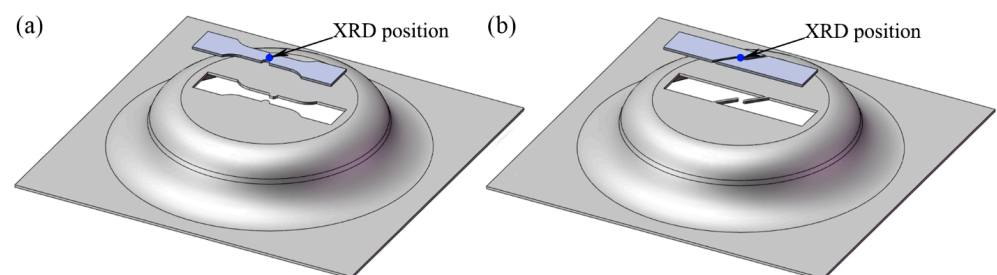


Figure 22. Specimens for the second-round deformation: (a) mini notched specimen; (b) mini pure shear specimen.

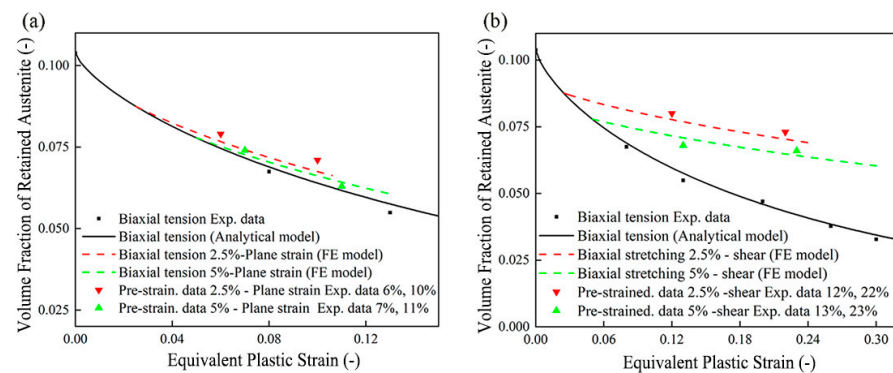


Figure 23. Distribution of retained austenite with varying EPS under different loading paths: (a) Comparison of the experimental results of the VFRA test and the VFRA prediction results of the FE model under Biaxial tension-plane strain tension at 6%, 10%, 7%, and 11% EPS. (b) Comparison of the experimental results of the VFRA test and the VFRA prediction results of the FE model under Biaxial tension-pure shear at 12%, 22%, 13%, and 23% EPS.

6. Conclusions

The martensitic transformation behavior under different temperatures, strain rates, and stress states is analyzed. The martensitic transformation kinetic model is developed based on microscopic characterization. The stress-strain model considering the phase transformation is implemented in the FE simulation, and its feasibility is verified by comparing with the experimental data. Finally, the user subroutine VUMAT is implemented in ABAQUS/Explicit to describe the martensitic transformation during the complex loading path test.

A phase transformation kinetic model considering temperature, strain rate, and stress state is developed. As the temperature goes up, the amount of martensitic transformation declines. The martensitic transformation rate increases sequentially in the order of pure shear, uniaxial tension, plane strain, and biaxial tension. The phase transformation is more complicatedly affected by strain rate. The increase of the strain rate will inhibit the phase transformation at $\dot{\epsilon} < 0.1/s$, while the increase will promote the phase transformation at $\dot{\epsilon} > 0.1/s$.

The deformation mode has a significant effect on the martensitic transformation behavior of QP steel which is induced by strain. This different transformation behavior changes the microstructure characteristics, which is invoked by the volume fraction of the newly transformed martensite. Therefore, the difference in martensitic transformation leads to the difference in flow stress under different deformation modes. The magnitude of the stress state influence on the strain hardening is ascending with increase of the stress triaxiality: pure shear ($\eta = 0.0344$), uniaxial tension ($\eta = 0.3343$), plane strain ($\eta = 0.5391$) and biaxial tension ($\eta = 0.6653$).

The martensitic transformation behavior of QP steel under linear/nonlinear strain paths is analyzed by designing cyclic and complex loading tests. The martensitic transformation rate of QP steel under cyclic shear loading and plane strain loading was similar to the one without cyclic loading, even in case of the reverse loading as the cyclic shear loading test does. It indicates that in the same stress state, the martensitic transformation closely depends on the EPS without taking into account how temperature and strain rate could affect. But if the specimen experiences nonlinear strain paths, such as the biaxial–uniaxial/shear loading, the martensitic transformation rate of QP steel is obviously influenced by nonlinear strain paths, such as the prestrain of the biaxial tension, stress state and the EPS of the second-round deformation. The proposed martensitic transformation model is capable of predicting the complex microstructural evolutions. Through the application of QP steel with its characteristic strain-induced martensitic transformation, we can obtain products with favorable strength and ductility characteristics. These properties make QP steel suit-

able for potential applications in body parts such as car body beams, bumper beams, and roof reinforcement beams, based on their anticipated applications for body parts.

Author Contributions: Conceptualization, B.T.; methodology, Z.L. and B.T.; software, Z.L.; validation, Z.L., B.T. and E.D.; formal analysis, E.D.; investigation, P.Y.; resources, B.T.; data curation, Z.L. and E.D.; writing—original draft preparation, Z.L.; writing—review and editing, B.T.; visualization, G.L.; supervision, N.G.; project administration, B.T.; funding acquisition, B.T. All authors have read and agreed to the published version of the manuscript.

Funding: This research was funded by the National Natural Science Foundation of China grant number (#52275344, #52105370), the Natural Science Foundation of Shandong Province (#ZR2020KE021, #ZR2020QE168), Taishan Industry Leading Talent Project (#TSL20221101), and Innovation Team of Jinan (#2019GXRC035).

Data Availability Statement: Not applicable.

Acknowledgments: We would like to express our sincere appreciation to Zhe Liu for his valuable contributions to this research. Liu's extensive knowledge and expertise in theoretical analysis and modeling were instrumental in shaping the core concepts of this work. His insights and recommendations have been invaluable to the success of this project.

Conflicts of Interest: The authors declare no conflict of interest.

Appendix A

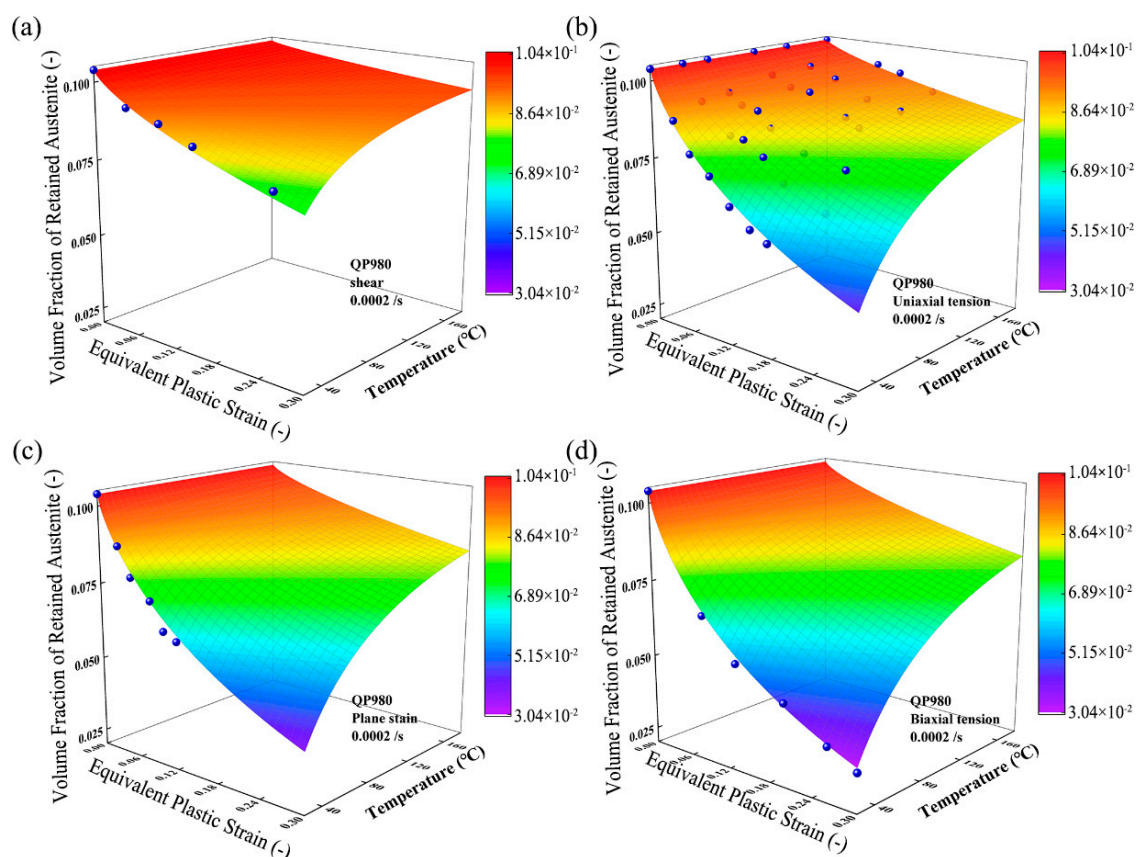


Figure A1. Retained austenite evolution with EPS and temperature in various stress conditions: (a) shear; (b) uniaxial tension; (c) plain strain; (d) biaxial tension (The blue balls are the experimental data).

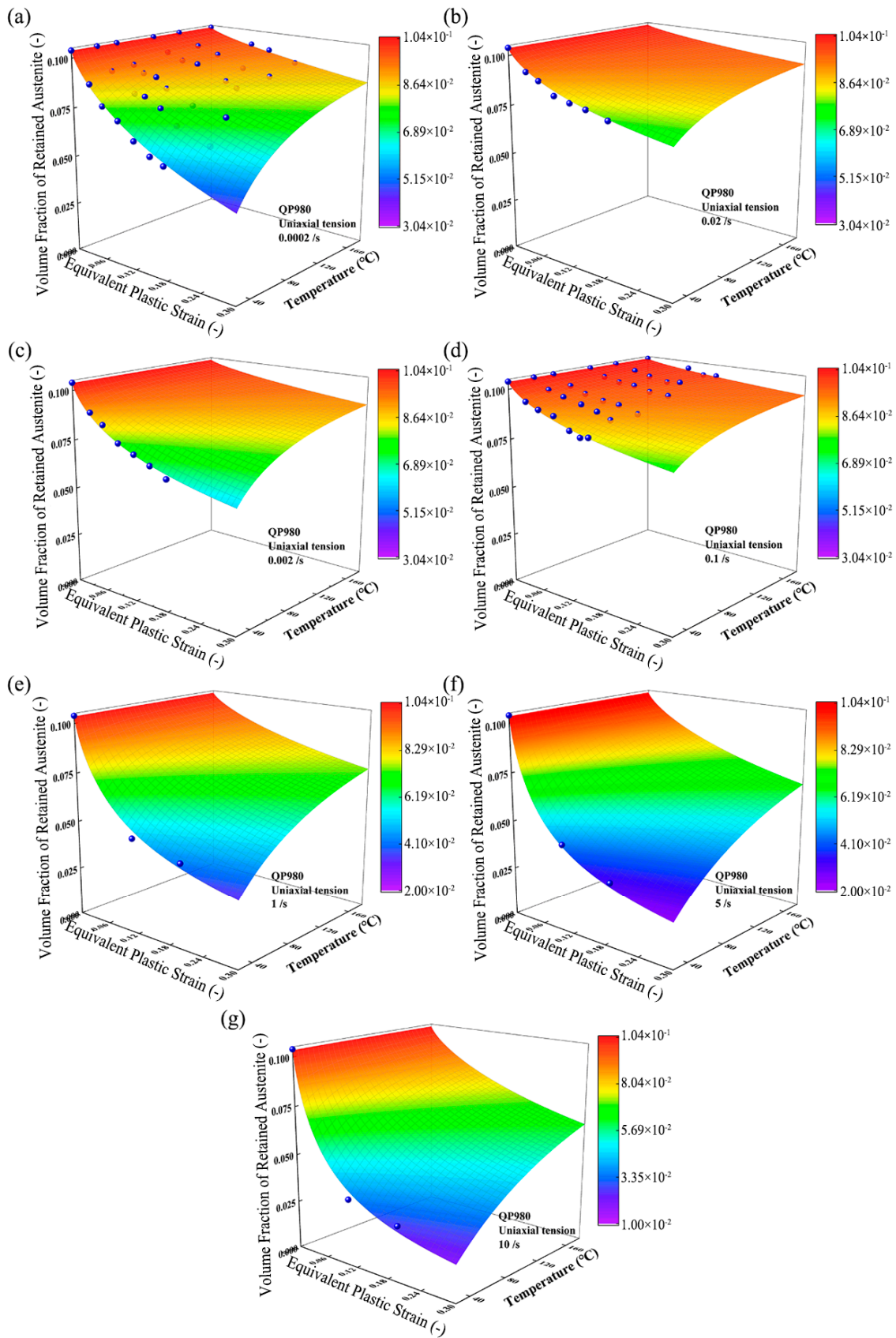


Figure A2. Retained austenite evolution with EPS and temperature at various strain rates: (a) 0.0002/s; (b) 0.002/s; (c) 0.02/s; (d) 0.1/s; (e) 1/s; (f) 5/s; (g) 10/s (The blue balls are the experimental data).

References

1. De Cooman, B. Structure–properties relationship in TRIP steels containing carbide-free bainite. *Curr. Opin. Solid State Mater. Sci.* **2004**, *8*, 285–303. [[CrossRef](#)]
2. Matlock, D.K.; Bräutigam, V.E.; Speer, J.G. Application of the Quenching and Partitioning (Q&P) Process to a Medium-Carbon, High-Si Microalloyed Bar Steel. *Mater. Sci. Forum* **2003**, *426–432*, 1089–1094. [[CrossRef](#)]
3. Speer, J.; Matlock, D.K.; De Cooman, B.C.; Schroth, J.G. Carbon partitioning into austenite after martensite transformation. *Acta Mater.* **2003**, *51*, 2611–2622. [[CrossRef](#)]
4. Zhang, W.; Xu, J. Advanced lightweight materials for Automobiles: A review. *Mater. Des.* **2022**, *221*, 110994. [[CrossRef](#)]
5. Grajcar, A.; Skowronek, A.; Radwański, K. Mechanical behavior and stability of dispersed retained austenite in thermomechanically rolled and isothermally-treated TRIP-aided multiphase steel. *Mater. Sci. Eng. A* **2022**, *830*, 142300. [[CrossRef](#)]
6. Hojo, T.; Koyama, M.; Kumai, B.; Shibayama, Y.; Shiro, A.; Shobu, T.; Saitoh, H.; Ajito, S.; Akiyama, E. Comparative study of stress and strain partitioning behaviors in medium manganese and transformation-induced plasticity-aided bainitic ferrite steels. *Scr. Mater.* **2022**, *210*, 114463. [[CrossRef](#)]
7. Sakuma, Y.; Matsumura, O.; Akisue, O. Influence of C Content and annealing Temperature on Microstructure and Mechanical Properties of 400.DEG.C. Transformed Steel Containing Retained Austenite. *ISIJ Int.* **1991**, *31*, 1348–1353. [[CrossRef](#)]
8. Zhang, G.-T.; Zhu, N.-Q.; Sun, B.-W.; Zhao, Z.-Z.; Zheng, Z.-W.; Tang, D.; Li, L. Effect of V Addition on Microstructure and Mechanical Properties in C–Mn–Si Steels after Quenching and Partitioning Processes. *Metals* **2021**, *11*, 1306. [[CrossRef](#)]
9. An, X.; Liu, Z.; Zhang, Y.; Wei, W.; Bai, J.; Xu, Z.; Hu, J.; Wei, K.; Chu, C.; Sun, W. Mechanical property regulation of transformation induced plasticity (TRIP) multi-principal element alloys through multi-phase microstructural design. *Intermetallics* **2023**, *152*, 107754. [[CrossRef](#)]
10. Muránsky, O.; Šittner, P.; Zrník, J.; Oliver, E. In situ neutron diffraction investigation of the collaborative deformation–transformation mechanism in TRIP-assisted steels at room and elevated temperatures. *Acta Mater.* **2008**, *56*, 3367–3379. [[CrossRef](#)]
11. Angel, T. Formation of martensite in austenitic stainless steels. *J. Iron Steel Inst.* **1954**, *177*, 165–174.
12. Ludwigson, D.C.; Berger, J.A. Plastic behaviour of metastable austenitic stainless steels. *J. Iron Steel Inst.* **1969**, *207*, 63–69.
13. Sugimoto, K.-I.; Kobayashi, M.; Hashimoto, S.-I. Ductility and strain-induced transformation in a high-strength transformation-induced plasticity-aided dual-phase steel. *Met. Mater. Trans. A* **1992**, *23*, 3085–3091. [[CrossRef](#)]
14. Sugimoto, K.-I.; Misu, M.; Kobayashi, M.; Shirasawa, H. Effects of Second Phase Morphology on Retained Austenite Morphology and Tensile Properties in a TRIP-aided Dual-phase Steel Sheet. *ISIJ Int.* **1993**, *33*, 775–782. [[CrossRef](#)]
15. Shin, H.C.; Ha, T.K.; Chang, Y.W. Kinetics of deformation induced martensitic transformation in a 304 stainless steel. *Scr. Mater.* **2001**, *45*, 823–829. [[CrossRef](#)]
16. Beese, A.M.; Mohr, D. Effect of stress triaxiality and Lode angle on the kinetics of strain-induced austenite-to-martensite transformation. *Acta Mater.* **2011**, *59*, 2589–2600. [[CrossRef](#)]
17. Olson, G.; Cohen, M. A mechanism for the strain-induced nucleation of martensitic transformations. *J. Less Common Met.* **1972**, *28*, 107–118. [[CrossRef](#)]
18. Olson, G.B.; Cohen, M. Kinetics of strain-induced martensitic nucleation. *Met. Mater. Trans. A* **1975**, *6*, 791–795. [[CrossRef](#)]
19. Stringfellow, R.; Parks, D.; Olson, G. A constitutive model for transformation plasticity accompanying strain-induced martensitic transformations in metastable austenitic steels. *Acta Met. Mater.* **1992**, *40*, 1703–1716. [[CrossRef](#)]
20. Tomita, Y.; Iwamoto, T. Constitutive modeling of trip steel and its application to the improvement of mechanical properties. *Int. J. Mech. Sci.* **1995**, *37*, 1295–1305. [[CrossRef](#)]
21. Iwamoto, T.; Tsuta, T.; Tomita, Y. Investigation on deformation mode dependence of strain-induced martensitic transformation in trip steels and modelling of transformation kinetics. *Int. J. Mech. Sci.* **1998**, *40*, 173–182. [[CrossRef](#)]
22. Tomita, Y.; Iwamoto, T. Computational prediction of deformation behavior of TRIP steels under cyclic loading. *Int. J. Mech. Sci.* **2001**, *43*, 2017–2034. [[CrossRef](#)]
23. Li, S.; Dan, W.; Zhang, W.; Lin, Z. A model for strain-induced martensitic transformation of TRIP steel with pre-strain. *Comput. Mater. Sci.* **2007**, *40*, 292–299. [[CrossRef](#)]
24. Kim, H.; Lee, J.; Barlat, F.; Kim, D.; Lee, M.-G. Experiment and modeling to investigate the effect of stress state, strain and temperature on martensitic phase transformation in TRIP-assisted steel. *Acta Mater.* **2015**, *97*, 435–444. [[CrossRef](#)]
25. Jiménez, J.A.; Carsí, M.; Ruano, O.; Frommeyer, G. Effect of testing temperature and strain rate on the transformation behaviour of retained austenite in low-alloyed multiphase steel. *Mater. Sci. Eng. A* **2009**, *508*, 195–199. [[CrossRef](#)]
26. Choi, K.; Liu, W.; Sun, X.; Khaleel, M. Microstructure-based constitutive modeling of TRIP steel: Prediction of ductility and failure modes under different loading conditions. *Acta Mater.* **2009**, *57*, 2592–2604. [[CrossRef](#)]
27. Hauser, M.; Wendler, M.; Fabrichnaya, O.; Volkova, O.; Mola, J. Anomalous stabilization of austenitic stainless steels at cryogenic temperatures. *Mater. Sci. Eng. A* **2016**, *675*, 415–420. [[CrossRef](#)]
28. Huang, F.; Yang, J.; Guo, Z.; Rong, Y.; Chen, N. Dynamic compression property of a low-carbon quenching and partitioning steel. *Mater. Sci. Eng. A* **2016**, *651*, 224–232. [[CrossRef](#)]
29. Moor, E.D.; Lacroix, S.; Clarke, A.J.; Penning, J.; Speer, J.G. Effect of Retained Austenite Stabilized via Quench and Partitioning on the Strain Hardening of Martensitic Steels. *Metall Mater. Trans. A* **2008**, *39*, 2586–2595. [[CrossRef](#)]
30. Feng, W.; Wu, Z.; Wang, L.; Speer, J.G. Effect of Testing Temperature on Retained Austenite Stability of Cold Rolled CMnSi Steels Treated by Quenching and Partitioning Process. *Steel Res. Int.* **2013**, *84*, 246–252. [[CrossRef](#)]

31. Hecker, S.S.; Stout, M.G.; Staudhammer, K.P.; Smith, J.L. Effects of Strain State and Strain Rate on Deformation-Induced Transformation in 304 Stainless Steel: Part I. Magnetic Measurements and Mechanical Behavior. *Met. Mater. Trans. A* **1982**, *13*, 619–626. [[CrossRef](#)]
32. Jacques, P.; Furnémont, Q.; Lani, F.; Pardoën, T.; Delannay, F. Multiscale mechanics of TRIP-assisted multiphase steels: I. Characterization and mechanical testing. *Acta Mater.* **2007**, *55*, 3681–3693. [[CrossRef](#)]
33. Serri, J.; Cherkaoui, M. Constitutive Modeling and Finite Element Analysis of the Formability of TRIP Steels. *J. Eng. Mater. Technol.* **2008**, *130*, 31009. [[CrossRef](#)]
34. Beese, A.; Mohr, D. Identification of the Direction-Dependency of the Martensitic Transformation in Stainless Steel Using In Situ Magnetic Permeability Measurements. *Exp. Mech.* **2010**, *51*, 667–676. [[CrossRef](#)]
35. Shan, T.; Li, S.; Zhang, W.; Xu, Z. Prediction of martensitic transformation and deformation behavior in the TRIP steel sheet forming. *Mater. Des.* **2008**, *29*, 1810–1816. [[CrossRef](#)]
36. Ishimaru, E.; Hamasaki, H.; Yoshida, F. Deformation-induced martensitic transformation behavior of type 304 stainless steel sheet in draw-bending process. *J. Mater. Process. Technol.* **2015**, *223*, 34–38. [[CrossRef](#)]
37. Zou, D.; Li, S.; He, J.; Gu, B.; Li, Y. The deformation induced martensitic transformation and mechanical behavior of quenching and partitioning steels under complex loading process. *Mater. Sci. Eng. A* **2018**, *715*, 243–256. [[CrossRef](#)]
38. Araki, K.; Takada, Y.; Nakaoka, K. Work Hardening of Continuously Annealed Dual Phase Steels. *Trans. Iron Steel Inst. Jpn.* **1977**, *17*, 710–717. [[CrossRef](#)]
39. Tomota, Y.; Nakamura, S.; Kuroki, K.; Tamura, I. On the average internal stresses in each constituent phase in plastically deformed two-ductile-phase alloys. *Mater. Sci. Eng.* **1980**, *46*, 69–74. [[CrossRef](#)]
40. Tsuchida, N.; Tomota, Y. A micromechanic modeling for transformation induced plasticity in steels. *Mater. Sci. Eng. A* **2000**, *285*, 346–352. [[CrossRef](#)]
41. Weng, G. The overall elastoplastic stress-strain relations of dual-phase metals. *J. Mech. Phys. Solids* **1990**, *38*, 419–441. [[CrossRef](#)]
42. Li, J.; Weng, G. A secant-viscosity approach to the time-dependent creep of an elastic viscoplastic composite. *J. Mech. Phys. Solids* **1997**, *45*, 1069–1083. [[CrossRef](#)]
43. Perlade, A.; Bouaziz, O.; Furnémont, Q. A physically based model for TRIP-aided carbon steels behaviour. *Mater. Sci. Eng. A* **2003**, *356*, 145–152. [[CrossRef](#)]
44. Han, H.N.; Gil Lee, C.; Oh, C.-S.; Lee, T.-H.; Kim, S.-J. A model for deformation behavior and mechanically induced martensitic transformation of metastable austenitic steel. *Acta Mater.* **2004**, *52*, 5203–5214. [[CrossRef](#)]
45. Fu, B.; Yang, W.; Wang, Y.; Li, L.; Sun, Z.; Ren, Y. Micromechanical behavior of TRIP-assisted multiphase steels studied with in situ high-energy X-ray diffraction. *Acta Mater.* **2014**, *76*, 342–354. [[CrossRef](#)]
46. Srivastava, A.; Ghassemi-Armaki, H.; Sung, H.; Chen, P.; Kumar, S.; Bower, A.F. Micromechanics of plastic deformation and phase transformation in a three-phase TRIP-assisted advanced high strength steel: Experiments and modeling. *J. Mech. Phys. Solids* **2015**, *78*, 46–69. [[CrossRef](#)]
47. Hou, Y.; Min, J.; Guo, N.; Shen, Y.; Lin, J. Evolving asymmetric yield surfaces of quenching and partitioning steels: Characterization and modeling. *J. Mater. Process. Technol.* **2021**, *290*, 116979. [[CrossRef](#)]
48. Min, J.; Kong, J.; Hou, Y.; Liu, Z.; Lin, J. Application of Laser Deposition to Mechanical Characterization of Advanced High Strength Steels Subject to Non-Proportional Loading. *Exp. Mech.* **2022**, *62*, 685–700. [[CrossRef](#)]
49. Hou, Y.; Lee, M.-G.; Lin, J.; Min, J. Experimental characterization and modeling of complex anisotropic hardening in quenching and partitioning (Q&P) steel subject to biaxial non-proportional loadings. *Int. J. Plast.* **2022**, *156*, 103347. [[CrossRef](#)]
50. Chakrabarty, S.; Bhargava, M.; Narula, H.K.; Pant, P.; Mishra, S.K. Prediction of strain path and forming limit curve of AHSS by incorporating microstructure evolution. *Int. J. Adv. Manuf. Technol.* **2020**, *106*, 5085–5098. [[CrossRef](#)]
51. Rittel, D.; Ravichandran, G.; Venkert, A. The mechanical response of pure iron at high strain rates under dominant shear. *Mater. Sci. Eng. A* **2006**, *432*, 191–201. [[CrossRef](#)]
52. Yang, B.; Dong, Y.; Guo, D.; Yang, C.; Zhang, X.; Peng, Y.; Wu, L.; Shi, B. Anisotropic mechanical behavior and corresponding microstructure evolution of extruded AZ31 under combined normal/shear stress states. *Mater. Sci. Eng. A* **2019**, *760*, 415–425. [[CrossRef](#)]
53. Daroju, S.; Kuwabara, T.; Knezevic, M. Experimental characterization and crystal plasticity modeling of dual-phase steels subjected to strain path reversals. *Mech. Mater.* **2022**, *168*, 104293. [[CrossRef](#)]
54. Wei, X.; Liu, Y.; Zhang, X. Effect of non-linear tension-compression loading reversal on the hardening behavior and initiation fracture strain of a cold-rolled TRIP780 steel sheet. *Mater. Today Commun.* **2022**, *30*, 103076. [[CrossRef](#)]
55. Rebergue, G.; Blaysat, B.; Chanal, H.; Duc, E. In situ measurement of machining part deflection with Digital Image Correlation. *Measurement* **2022**, *187*, 110301. [[CrossRef](#)]
56. Beese, A.M.; Mohr, D. Anisotropic plasticity model coupled with Lode angle dependent strain-induced transformation kinetics law. *J. Mech. Phys. Solids* **2012**, *60*, 1922–1940. [[CrossRef](#)]
57. Xu, H.J.; Jin, S.Y.; Zheng, B.R. New Technique of Petrofabric: Electron Backscatter Diffraction (EBSD). *Fac. Earth Sci.* **2007**, *21*, 213–225. Available online: <http://www.geoscience.net.cn/EN/Y2007/V21/I2/213> (accessed on 1 January 2020).
58. De, A.K.; Murdock, D.C.; Mataya, M.C.; Speer, J.G.; Matlock, D.K. Quantitative measurement of deformation-induced martensite in 304 stainless steel by X-ray diffraction. *Scr. Mater.* **2004**, *50*, 1445–1449. [[CrossRef](#)]

59. Hetzner, D.W. X-ray Determination of Retained Austenite in Steel Using ASTM E975. *Microsc. Microanal.* **2003**, *9*, 710–711. [[CrossRef](#)]
60. Zhou, S.; Zhong, Y.; Wang, L. Research and applications of 1.2 GPa quenching and partitioning (Q&P) steel. *Baosteel Technical Research.* **2016**, *6*, 36–41. [[CrossRef](#)]
61. Thomas, G.; Speer, J.; Matlock, D.; Michael, J. Application of Electron Backscatter Diffraction Techniques to Quenched and Partitioned Steels. *Microsc. Microanal.* **2011**, *17*, 368–373. [[CrossRef](#)] [[PubMed](#)]
62. De Knijf, D.; Petrov, R.; Föjer, C.; Kestens, L.A. Effect of fresh martensite on the stability of retained austenite in quenching and partitioning steel. *Mater. Sci. Eng. A* **2014**, *615*, 107–115. [[CrossRef](#)]
63. Sherif, M.Y.; Garcia-Mateo, C.; Sourmail, T.; Bhadeshia, H.K.D.H. Stability of retained austenite in TRIP-assisted steels. *Mater. Sci. Technol.* **2004**, *20*, 319–322. [[CrossRef](#)]
64. Li, S.; Zou, D.; Xia, C.; He, J. Effect of Strain Rate on Deformation-Induced Martensitic Transformation of Quenching and Partitioning Steels. *Steel Res. Int.* **2016**, *87*, 1302–1311. [[CrossRef](#)]
65. Zou, D.; Li, S.; He, J. Temperature and strain rate dependent deformation induced martensitic transformation and flow behavior of quenching and partitioning steels. *Mater. Sci. Eng. A* **2017**, *680*, 54–63. [[CrossRef](#)]
66. He, J.; Han, G.; Feng, Y. Phase transformation and plastic behavior of QP steel sheets: Transformation kinetics-informed modeling and forming limit prediction. *Thin-Walled Struct.* **2022**, *173*, 108977. [[CrossRef](#)]
67. Tang, B.; Wu, F.; Guo, N.; Liu, J.; Ge, H.; Bruschi, S.; Li, X. Numerical modeling of ductile fracture of hot stamped 22MnB5 boron steel parts in three-point bending. *Int. J. Mech. Sci.* **2020**, *188*, 105951. [[CrossRef](#)]
68. Mohapatra, S.; Poojari, G.; Marandi, L.; Das, S.; Das, K. A systematic study on microstructure evolution, mechanical stability and the micro-mechanical response of tensile deformed medium manganese steel through interrupted tensile test. *Mater. Charact.* **2023**, *195*, 112562. [[CrossRef](#)]
69. Brosius, A.; Yin, Q.; Güner, A.; Tekkaya, A. A New Shear Test for Sheet Metal Characterization. *Steel Res. Int.* **2011**, *82*, 323–328. [[CrossRef](#)]
70. Yin, Q.; Soyarslan, C.; Güner, A.; Brosius, A.; Tekkaya, A. A cyclic twin bridge shear test for the identification of kinematic hardening parameters. *Int. J. Mech. Sci.* **2012**, *59*, 31–43. [[CrossRef](#)]

Disclaimer/Publisher’s Note: The statements, opinions and data contained in all publications are solely those of the individual author(s) and contributor(s) and not of MDPI and/or the editor(s). MDPI and/or the editor(s) disclaim responsibility for any injury to people or property resulting from any ideas, methods, instructions or products referred to in the content.